A Comparison of the Stellar, CO, and Dust-continuum Emission from Three Star-forming HUDF Galaxies at $z \sim 2$

Melanie Kaasinen[1,2,3] , Fabian Walter[1] , Mladen Novak[1] , Marcel Neeleman[1] , Ian Smail[4] , Leindert Boogaard[5] ,
Elisabete da Cunha[3,6,7] , Axel Weiss[8] , Daizhong Liu[1] , Roberto Decarli[9] , Gergö Popping[10] , Tanio Diaz-Santos[11,12,13] ,
Paulo Cortés[14,15] , Manuel Aravena[11] , Paul van der Werf[5] , Dominik Riechers[1,16] , Hanae Inami[17] ,
Jacqueline A. Hodge[5] , Hans-Walter Rix[1] , and Pierre Cox[18]

[1] Max-Planck-Institut für Astronomie, Königstuhl 17, D-69117 Heidelberg, Germany; kaasinen@mpia.de
[2] Universität Heidelberg, Zentrum für Astronomie, Institut für Theoretische Astrophysik, Albert-Ueberle-Straße 2, D-69120 Heidelberg, Germany
[3] ARC Centre of Excellence for All Sky Astrophysics in 3 Dimensions (ASTRO 3D), Australia
[4] Centre for Extragalactic Astronomy, Department of Physics, Durham University, Durham DH1 3LE, UK
[5] Leiden Observatory, Leiden University, P.O. Box 9513, NL-2300 RA Leiden, The Netherlands
[6] International Centre for Radio Astronomy Research, University of Western Australia, 35 Stirling Hwy, Crawley, WA 6009, Australia
[7] Research School of Astronomy and Astrophysics, The Australian National University, Canberra, ACT 2611, Australia
[8] Max-Planck-Institut für Radioastronomie, Auf dem Hügel 69, D-53121 Bonn, Germany
[9] INAF—Osservatorio di Astrofisica e Scienza dello Spazio di Bologna, via Gobetti 93/3, I-40129, Bologna, Italy
[10] European Southern Observatory, Karl-Schwarzschild-Strasse 2, D-85748, Garching, Germany
[11] Núcleo de Astronomía, Facultad de Ingeniería y Ciencias, Universidad Diego Portales, Ejército Libertador 441, Santiago 8320000, Chile
[12] Institute of Astrophysics, Foundation for Research and Technology-Hellas (FORTH), Heraklion, GR-70013, Greece
[13] Chinese Academy of Sciences South America Center for Astronomy (CASSACA), National Astronomical Observatories, CAS, Beijing 100101, People's Republic of China
[14] Joint ALMA Observatory—ESO, Av. Alonso de Córdova, 3107, Santiago, Chile
[15] National Radio Astronomy Observatory, 520 Edgemont Rd, Charlottesville, VA, 22903, USA
[16] Department of Astronomy, Cornell University, Space Sciences Building, Ithaca, NY 14853, USA
[17] Hiroshima Astrophysical Science Center, Hiroshima University, 1-3-1 Kagamiyama, Higashi-Hiroshima, Hiroshima 739-8526, Japan
[18] Institut dastrophysique de Paris, Sorbonne Université, CNRS, UMR 7095, 98 bis bd Arago, F-7014 Paris, France

Abstract

We compare the extent of the dust, molecular gas, and stars in three star-forming galaxies, at $z = 1.4$, 1.6, and 2.7, selected from the Hubble Ultra Deep Field based on their bright carbon monoxide (CO) and dust-continuum emission as well as their large rest-frame optical sizes. The galaxies have high stellar masses, $M_* > 10^{11} M_\odot$, and reside on, or slightly below, the main sequence of star-forming galaxies at their respective redshifts. We probe the dust and molecular gas using subarcsecond Atacama Large Millimeter/submillimeter Array observations of the 1.3 mm continuum and CO line emission, respectively, and probe the stellar distribution using *Hubble Space Telescope* observations at 1.6 μm. We find that for all three galaxies the CO emission appears $\gtrsim$30% more compact than the stellar emission. For the $z = 1.4$ and 2.7 galaxies, the dust emission is also more compact, by $\gtrsim$50%, than the stellar emission, whereas for the $z = 1.6$ galaxy, the dust and stellar emission have similar spatial extents. This similar spatial extent is consistent with observations of local disk galaxies. However, most high-redshift observations show more compact dust emission, likely because of the ubiquity of central starbursts at high redshift and the limited sensitivity of many of these observations. Using the CO emission line, we also investigate the kinematics of the cold interstellar medium in the galaxies, and find that all three have kinematics consistent with a rotation-dominated disk.

Unified Astronomy Thesaurus concepts: High-redshift galaxies (2034); Interstellar medium (847); Dust-continuum emission (412); Galaxy evolution (594); Molecular gas (1073)

1. Introduction

The molecular gas phase of the interstellar medium (ISM) is a crucial component of star-forming galaxies, hosting and providing the fuel for star formation. Constraining the spatial distribution of both stars and molecular gas is therefore critical to understanding the evolutionary state of a galaxy. Whereas the stellar component of a galaxy is best traced via the rest-frame near-infrared emission, molecular gas is most commonly observed via carbon monoxide (CO) line emission or far-infrared (FIR) dust-continuum emission. These stellar and molecular gas tracers have been mapped at high resolution (down to 100 pc scales) for local galaxies (e.g., Leroy et al. 2008; Sandstrom et al. 2013; Schinnerer et al. 2019), providing fundamental insights into the physics of star formation and the

matter cycle of the ISM. However, such detailed, multi-wavelength comparisons are still lacking for galaxies at the peak epoch of stellar mass assembly, at $z \sim 2$.

The advent of sub/millimeter interferometers, particularly the Atacama Large Millimeter/submillimeter Array (ALMA) and NOrthern Extended Millimeter Array, have led to a growing body of work aimed at characterizing the molecular gas properties of $z \gtrsim 2$ galaxies via their CO and/or dust-continuum emission (e.g., surveys described in Walter et al. 2016; Scoville et al. 2017; Pavesi et al. 2018; Tacconi et al. 2018; Decarli et al. 2019; Stach et al. 2019). Based on unresolved measurements, the long-wavelength (observed-frame 850 μm), dust-continuum emission appears to trace the bulk of the cold, molecular gas in massive, star-forming galaxies as accurately as the traditional tracer, CO(1–0)

(Scoville et al. 2014; Kaasinen et al. 2019). However, resolved observations indicate that the dust-continuum emission stems from a significantly more compact region than the CO emission (e.g., Hodge et al. 2015; Simpson et al. 2015; Chen et al. 2017; Calistro Rivera et al. 2018; Gullberg et al. 2019), calling into question its application as a molecular gas tracer.

To date, the sizes of the rest-frame optical, dust-continuum, and CO emitting regions have been compared for only the brightest and most massive high-redshift ($z > 1$) sources. For $z \sim 2$–4 submillimeter-selected galaxies (SMGs; Blain et al. 2002), the measured dust-continuum emission appears 2–4 times more compact than the CO emission (Hodge et al. 2015; Simpson et al. 2015; Chen et al. 2017; Calistro Rivera et al. 2018). Similarly, for quasar host galaxies at $z \gtrsim 6$ (studied with lower-resolution observations), the dust-continuum sizes also appear $z \sim 2$–4 times more compact than those of the CO (Feruglio et al. 2018; Wang et al. 2019). The dust-continuum and rest-frame optical (but not CO) sizes have also been compared in detail for SMGs (Hodge et al. 2016, 2019; Gullberg et al. 2019; Lang et al. 2019); six massive and compact star-forming galaxies at $z \sim 2.5$ (Barro et al. 2016); a $z \sim 1.25$ starburst (Nelson et al. 2019); and massive, Hα-selected galaxies at $z \sim 2.2$–2.5 (Tadaki et al. 2017a). These studies all find that the dust emission is 2–4 times more compact than the rest-frame optical emission.

It is still unclear how the spatial extents of the stellar, dust-continuum, and CO emission compare for the wider population of star-forming galaxies, including the population conforming to the so-called main sequence (MS) of star-forming galaxies (the correlation between the stellar mass and star formation rate (SFR) of the majority of star-forming galaxies observed for each epoch up to $z \sim 4$, e.g., in Noeske et al. 2007; Salmi et al. 2012; Whitaker et al. 2012, 2014; Schreiber et al. 2016). In the first study of MS galaxies, Tadaki et al. (2017b) measure 1.5–2 times smaller dust-continuum versus CO half-light radii. However, the two massive ($M_* > 10^{11} M_\odot$) galaxies in their study were selected based on their compact, dusty, star-forming cores. An additional complication to the selection biases is that most previous observations of the dust-continuum emission of high-redshift sources have been conducted at infrared (IR) wavelengths, at which the dust luminosity is highly sensitive to the ISM temperature and thereby traces the star formation rate along with the dust reservoir. Moreover, few studies exist with resolved observations of both the CO and dust-continuum emission in unlensed objects (e.g., Hodge et al. 2015; Chen et al. 2017; Tadaki et al. 2017b; Calistro Rivera et al. 2018), of which only a subset are at a comparable resolution (Hodge et al. 2015; Calistro Rivera et al. 2018).

In this work, we test how the spatial extent (quantified by the half-light radii) of dust-continuum, CO, and rest-frame optical emission compare for three extended, MS galaxies at $z \sim 2$. To this end, we selected sources in the Hubble Ultra Deep Field (HUDF) for which the dust-continuum and CO emission have already been detected with ALMA as part of the ALMA Spectroscopic Survey in the Hubble Ultra Deep Field (ASPECS) Large Program (LP) (Aravena et al. 2019; Decarli et al. 2019; González-López et al. 2019). To best compare the spatial extents, we study the three sources with the most extended morphologies in the ultraviolet (UV) to near-IR images taken with the *Hubble Space Telescope* (HST). We use observations taken as part of the ALMA Spectroscopic Survey

in the Hubble Ultra Deep Field (ASPECS) LP as well as our "ASPECS Large Program Source" (ALPS) follow-up, higher-resolution ALMA observations. Thus, throughout this paper we refer to our sources as ALPS.1, 2, and 3. This paper is structured as follows. In Section 2 we describe the observations, data reduction, and imaging of the CO and dust-continuum emission. We discuss the global galaxy properties inferred from the multiwavelength data in Section 3. In Section 4, we derive and compare the half-light radii of the dust-continuum emission, CO, and rest-frame optical. We derive dynamical properties in Section 5 via kinematic modeling. We compare our sources to other samples in Section 6 and summarize our main findings in Section 7. Throughout this paper we assume a ΛCDM cosmology with $H_0 = 70$ km s^{-1} Mpc^{-1}, $\Omega_M = 0.3$, and $\Omega_\Lambda = 0.7$. Stellar masses and star formation rates are based on a Chabrier (2003) initial mass function. When quoting molecular gas masses we account for a factor of 1.36 to include He.

## 2. Sample Selection, Observation, and Data Reduction

2.1. Galaxy Selection

The three galaxies studied here are derived from the ASPECS LP, a survey of the sub-mm to mm emission within the HUDF (Decarli et al. 2019; González-López et al. 2019). Because the survey was conducted without preselection, it identified the sources brightest in CO line and dust-continuum emission. Based on the line searches performed by González-López et al. (2019), ASPECS provided 16 highly significant CO detections. From this sample of 16, we selected the three CO- and dust-brightest galaxies, with the most extended rest-frame optical emission. These two criteria were equally important. We required the sources to be CO-bright in order to resolve their emission, at $\sim 0\farcs 5$, within five hours of integration time, with ALMA, and select galaxies that are extended in the rest-frame optical to increase the chances of observing extended dust and CO emission. In Figure 1, we compare the properties of the three galaxies studied here to the parent sample of ASPECS LP 1.2 mm candidates (listed in Table 1 of González-López et al. 2020) and the full set of galaxies in the HUDF (see Aravena et al. 2020). Our ALPS sources have large stellar masses ($\gtrsim 10^{11} M_\odot$) and high FIR luminosities compared with the majority of the sources in the field, because of our selection of CO- and 1 mm-bright targets. Their extended and inclined rest-frame UV-optical morphologies are shown in the first three columns of Figure 2.

Compared to most observed SMGs, our galaxies have more extended morphologies in the rest-frame UV and optical emission. However, the interpolated 870 μm flux densities are consistent with the definition of an SMG, i.e., >1 mJy (see for discussions on the selection and classification Casey et al. 2014; Hodge & da Cunha 2020). Assuming that the FIR continuum can be described by a modified blackbody (MBB) with an average dust temperature of 25 K and a dust emissivity index of 1.8 (see Section 3.1), the 1.3 mm flux densities measured by González-López et al. (2020) extrapolate to 1.4 ± 0.1, 1.5 ± 0.1, and 2.8 ± 0.1 mJy for ALPS.1, 2, and 3 respectively. However, the FIR luminosities (bolometric luminosity between 8 and 1000 μm) of ALPS.1 and 2 are lower than what is typically measured for SMGs. Based on the models fit to the spectral energy distributions (SEDs), ALPS.1,
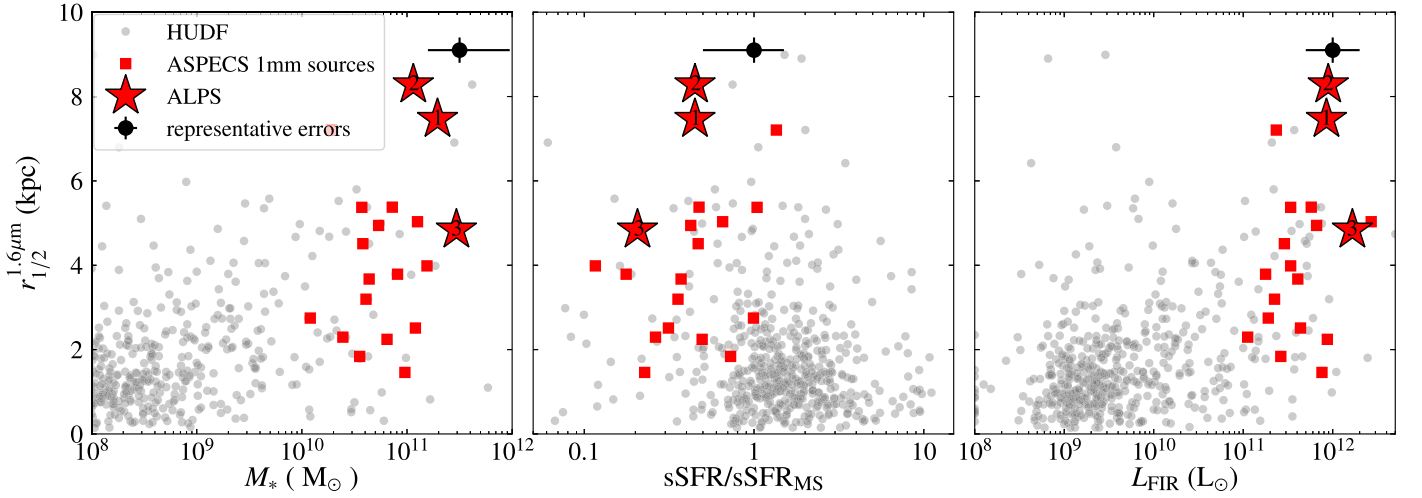
Figure 1. Comparison of the ALPS sample properties relative to the parent samples at $1 < z < 3$. The 1.6 μm (stellar) half-light radii are shown as a function of stellar mass M_*, offset from the MS and FIR luminosity (within 8–1000 μm) in the left, middle, and right panels, respectively. The three ALPS sources studied in this work (red stars) are compared with the ASPECS 1 mm continuum and line sources (red squares) and the HUDF sample (gray circles), from Aravena et al. (2020). The offset from the MS (in the middle panel) is calculated individually, based on the measured redshift, stellar mass, and SFR of each source, and, following Aravena et al. (2020), the MS is defined by the best-fit relation of Schreiber et al. (2015). The 1.6 μm half-light radii are from Table 2 of van der Wel et al. (2012) and were measured from the F160W maps. The three galaxies studied here were selected to be both extended in the rest-frame optical and to be CO- and FIR-bright. They also have large stellar masses and systematically lower specific SFRs (sSFR = SFR/M_*) than the majority of galaxies observed in the HUDF.
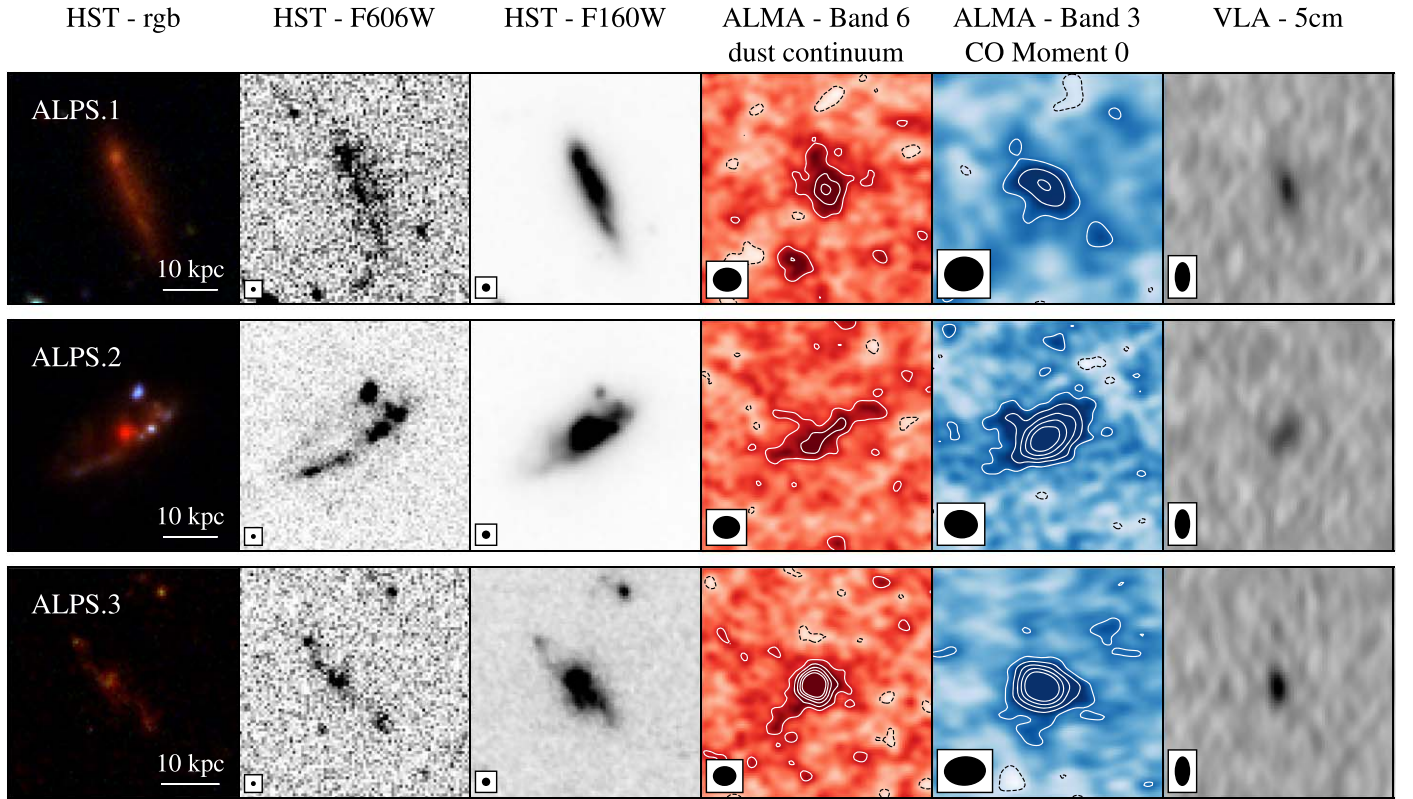
Figure 2. Multiwavelength data for the three observed sources (labeled ALPS.1, 2, and 3 at the upper left of the left panel in each row). Each panel depicts a $5'' \times 5''$ region centered on the kinematic center of the source. Columns, from left to right: HST 435-775-105 color composite, HST/F606W, HST/F160W, Band 6 (1.3 mm) dust continuum (combined ASPECS LP and Dunlop et al. 2017 data), CO moment-0 map (from the combined ASPECS LP and ALPS data) and Very Large Array (VLA)—5 cm continuum flux. The contours for the Band 6 dust continuum and CO moment 0 start at $\pm 2\sigma$ and change in steps of 2σ. Dashed black (solid white) lines show negative (positive) contours.

2, and 3 have FIR luminosities of $(0.78 \pm 0.04) \times 10^{12}$, $(0.9 \pm 0.1) \times 10^{12}$, and $(1.8 \pm 0.6) \times 10^{12} L_\odot$, respectively. SMGs have FIR luminosities of $L_{FIR} \gtrsim 10^{12} L_\odot$, typically

$\sim 3 \times 10^{12} L_\odot$ (e.g., Swinbank et al. 2014). Thus, ALPS.1 and 2 are at the faint end of the SMG population, whereas ALPS.3 is entirely consistent with most observed SMGs.

Table 1
Description of ALMA Observations

ALPS ID	ALPS.1	ALPS.2	ALPS.3
ASPECS LP 1 mm ID	1 mm.03	1 mm.05	1 mm.06
ASPECS LP 3 mm ID	3 mm.04	3 mm.05	3 mm.07
Dunlop et al. (2017) ID	UDF.6	UDF.8	UDF.2
R.A. (J2000)	03:32:34.44	03:32:39.77	03:32:43.53
Decl. (J2000)	−27:46:59.8	−27:46:11.8	−27:46:39.2
z_{CO}	1.4140	1.5504	2.6961
CO transition	$2 \rightarrow 1$	$2 \rightarrow 1$	$3 \rightarrow 2$
50 km s^{-1} CO Cube			
Weighting parameter	0.5	2	2
Beam FWHM ($'' \times ''$)	0.82×0.72	0.71×0.58	0.88×0.61
rms per channel (mJy beam^{-1})	0.14	0.09	0.11
Dust-continuum map (211–231 GHz; 1.3 mm)			
Weighting parameter	2	2	2
Beam FWHM ($'' \times ''$)	0.59×0.49	0.56×0.47	0.48×0.40
rms (μJy beam^{-1})	21	22	24

2.2. Dust-Continuum (Band 6) Observations

We analyze two Band 6 (211–275 GHz; 1.1–1.4 mm) surveys of the HUDF, taken at different depths and resolutions. We use the unresolved observations from the ASPECS LP (project code: 2016.1.00324, described in González-López et al. 2020) and the 1.3 mm observations of Dunlop et al. (2017) (project code: 2012.1.00173.S), which provide a higher spatial resolution. The source IDs from the ASPECS LP and HUDF data of Dunlop et al. (2017) are provided in Table 1. In the subsequent analysis (Section 2.4), we combine both data sets to achieve high resolution without the loss of large-scale emission. The ASPECS 1.3 mm observations, executed between 2017 March 10 and 2018 July 13, were conducted in the C43-3 configuration with a minimum baseline of 15 m and maximum baseline of 500 m. Our three sources lie toward the edges of the mosaic (where the primary beam responses are 87%, 65%, and 20% of the peak sensitivity, respectively, for ALPS.1, 2, and 3). Thus, the data for our sources are not as deep as those in the center of the mosaic. The Dunlop et al. (2017) observations were conducted in ALMA Cycle 2 using a variety of configurations, with maximum baselines between 550 and 1250 m (see Table 2 of Dunlop et al. 2017). The pointings of the ASPECS LP are more closely spaced than for the Dunlop et al. (2017) observations; however, the latter sample a larger area. Thus, for ALPS.3, on the edge of the ASPECS field, the majority of the data used here are from Dunlop et al. (2017).

2.3. CO Line (Band 3) Observations

To study the CO line emission of our three sources, we use two sets of ALMA Band 3 (84–115 GHz; 2.6–3.6 mm) data. We use the ASPECS LP Band 3 survey (project code: 2016.1.00324.L) and our targeted, follow-up ALPS observations, at higher resolution (project code: 2017.1.00270.S). The source IDs from the ASPECS LP are provided in Table 1 along with the CO-derived redshifts and observed CO transitions. An additional source was observed at the same redshift as, and at small angular separation to, ALPS.3 (ASPECS ID 3 mm.09), but was excluded from the main text work because of the lack of extended emission. We discuss this source further in Appendix A.

The ASPECS LP Band 3 observations are comprised of 17 pointings conducted in the compact, C40-3 configuration (with baselines ranging from 15 to 700 m). Further details are described in Decarli et al. (2019). For our sample, the sensitivity of the observations was the highest for ALPS.2 and lowest for ALPS.3 (with primary beam responses of 70%, 80%, and 50% of the peak sensitivity for ALPS.1, 2, and 3, respectively). In addition, we rely on new, supplementary, high-resolution Band 3 data, taken between 2018 January 4–11. These ALMA observations were conducted in the C43-5 configuration (minimum baseline of 15 m and maximum baseline of 2.5 km). The bandpass, flux, and phase calibrators were J0522-3627, J0329-2357, and J0342-3007, respectively.

2.4. Data Reduction and Imaging

All sets of raw data were reduced using the standard ALMA calibration scripts for the Common Astronomy Software Application (CASA; McMullin et al. 2007). For all sets of observations, the standard pipeline produced uv-data products of high quality and was therefore used without additional modifications. Following the raw data reduction, we combine the various sets of data for each band. The subsequent concatenating and imaging was carried out using CASA version 5.4.0.

2.4.1. Dust-Continuum (Band 6) Imaging

We image the dust continuum using the Band 6 data from the ASPECS LP (González-López et al. 2020) and from Dunlop et al. (2017). These two data sets cover different frequency ranges, i.e., the ASPECS LP data (González-López et al. 2020) span 212–272 GHz, whereas the Dunlop et al. (2017) data span 211–231 GHz, and were taken with different configurations. To probe the extended 1.3 mm emission at high resolution, and ensure that we are probing the same wavelengths at all radii, we select the four (out of 32) spectral windows from the ASPECS LP that match those of Dunlop et al. (2017). By subselecting these spectral windows from the ASPECS LP data, we reduce the depth of our observations relative to the LP. However, this selection is the best compromise between the sensitivity to extended emission and resolution required for our study. In effect this subselection is a form of tapering, which we use to avoid weighting the final maps to the large amount of short baseline measurements from the large program. We jointly image the two sets of uv-data via CASA's TCLEAN by applying the "mosaic" gridding option. To maximize the signal-to-noise ratio (S/N) of the final images, we image the data using a natural weighting scheme and clean to 2σ, within a circular mask of $3''$ radius. The cleaned maps, for each source, are shown in the 4th column of Figure 2, and their properties are summarized in Table 1. The comparative size of the synthesized beams reflects the relative contribution of the ASPECS LP versus Dunlop et al. (2017) data, with the beam size decreasing the farther a source lies toward the edge of the ASPECS 1 mm mosaic. ALPS.3 (at the very edge of the LP mosaic) has by far the smallest beam size, because most of the visibilities are from the Dunlop et al. (2017) data.

2.4.2. CO Line (Band 3) Imaging

To image the CO emission, we combine the low- and high-resolution data from the ASPECS LP Band 3 and ALPS programs. We initially attempt to subtract the continuum (via CASA's uvcontsub), but recover no significant continuum emission, rendering this step redundant. We image the uv-data

using CASA's TCLEAN task, mosaicing the pointings from the ASPECS LP and follow-up ALPS program via the "mosaic" gridding option and setting the phase center to the expected source center (the pointing of the ALPS data). We apply a circular mask of 3″ radius to create all cleaned images. We test a variety of robust weighting parameters to find the optimum balance between the resolution and resulting noise level. For the final images of ALPS.2 and 3 we use natural weighting, whereas for ALPS.1 we use robust weighting (see Table 1).

To create the moment-0 maps, from which we estimate source sizes, we create a single-channel image over the extent of the line emission, (the 99.99th percentile range, as in Aravena et al. 2019) applying the "multiscale" deconvolver (with a deconvolution scale of up to 2″) and cleaning down to a threshold of 2σ within a mask of radius 3″. We compare these moment-0 maps to maps obtained from 50 and 100 km s^{-1} data cubes, ensuring that the extent and morphology of the source emission in all moment-0 maps are consistent, but select the single-channel image for the moment-0 map to ensure that we have robust noise estimates.

3. Derived Global Quantities

3.1. Deriving Dust and Gas Masses from the ALMA Maps

We measure the total CO and dust-continuum flux densities from the cleaned, dirty, and residual maps by applying the residual scaling method (described in detail in Appendix A of Novak et al. 2019). This involves estimating the unknown, intrinsic flux by rescaling the contribution from the residual map with an estimate of the area of the dirty beam in the region of interest. The rescaling process is necessary to account for the ill-defined beam units of each cleaned interferometric map, which is a combination of the residual component in units of Jy per dirty beam, and a cleaned component in units of Jy per clean beam. For both the CO and dust-continuum emission, we extract the total flux densities from within circular apertures of 1″.5, 2″, and 1″.5 for ALPS.1, 2, and 3, respectively. We estimate the uncertainties of these flux densities as the local rms, σ, (in units of Jy beam^{-1}) scaled by the square root of the number of independent clean beams filling the aperture.

We compare the flux densities measured here (Table 2) to those derived using the ASPECS LP data only. Our CO emission line fluxes are consistent, within the uncertainties, with the spectral line fits of the unresolved ASPECS LP data, presented in Boogaard et al. (2020), and are 20% lower, on average, than the values in González-López et al. (2019) (although still consistent within errors). For ALPS.1 and 3, our 1.3 mm continuum flux density measurements are consistent with the measurements of Dunlop et al. (2017), whereas our value for ALPS.2 is $(50 \pm 20)\%$ larger. Conversely, the 1.3 mm flux density measured here for ALPS.1 is $(55 \pm 20)\%$ lower than the continuum flux density measured based on the ASPECS LP data in González-López et al. (2020), whereas the flux density measured for ALPS.3 is consistent within the errors. The 1.3 mm flux density measured here for ALPS.2 is consistent with the value in González-López et al. (2020). The difference between the flux densities measured by Dunlop et al. (2017) and González-López et al. (2020) can be mostly attributed to the different spectral setups, with the Dunlop et al. (2017) covering longer wavelengths. Similarly, the smaller flux density measured here for ALPS.1 is, in part, the result of the subselection of spectral setups.

Table 2
Derived Properties

Source	ALPS.1	ALPS.2	ALPS.3
SED fitting			
M_* ($10^{11}\ M_\odot$)	$1.9^{+1.9}_{-1.0}$	$1.1^{+2.2}_{-0.6}$	$3.0^{+3.0}_{-1.5}$
M_{dust}^{SED} ($10^8\ M_\odot$)	$1.1^{+0.3}_{-0.2}$	$1.6^{+0.1}_{-0.5}$	$7.8^{+1.2}_{-1.0}$
SFR ($M_\odot$ yr^{-1})	54^{+27}_{-13}	48^{+24}_{-12}	98^{+89}_{-25}
sSFR (Gyr^{-1})	$0.3^{+0.1}_{-0.1}$	$0.4^{+0.1}_{-0.1}$	$0.3^{+0.7}_{-0.4}$
sSFR/sSFR (Schreiber+2015)	0.4 ± 0.4	0.4 ± 0.4	0.2 ± 0.2
ξ_{AGN}		$0.15^{+0.04}_{-0.04}$	
Flux densities, applied ratios, and derived masses			
J_{obs}	2	2	3
$S_{CO}\Delta v$ (mJy km s^{-1})	600 ± 130	560 ± 80	560 ± 70
$L'_{CO}\ (J_{obs} - (J_{obs} - 1))$			
(10^{10} K km s^{-1} pc^2)	1.6 ± 0.3	1.7 ± 0.2	2.1 ± 0.3
$r_{J_{obs},1}$	0.8 ± 0.2	0.8 ± 0.2	0.79 ± 0.21
$L'_{CO(1-0)}$			
(10^{10} K km s^{-1} pc^2)	2.0 ± 0.3	2.2 ± 0.2	2.6 ± 0.3
α_{CO} [c]			
(M$_\odot$ / (K km s^{-1} pc^2))	3.9 ± 0.4	4.2 ± 0.4	4.1 ± 0.4
M_{mol} ($10^{11}\ M_\odot$)	0.8 ± 0.3	0.9 ± 0.3	1.1 ± 0.3
$S_{1.3\ mm}$ (μ Jy)	240 ± 70	400 ± 100	860 ± 120
$M_{dust}^{1.3\ mm}$ ($10^8\ M_\odot$)	2.4 ± 0.7	4.0 ± 1.0	7.6 ± 1.1
Inferred mass ratios			
$M_{mol}/M_{dust}^{1.3\ mm}$	320 ± 150	230 ± 90	140 ± 50
M_{mol}/M_*	0.4 ± 0.2	0.8 ± 0.5	0.4 ± 0.2

Notes.
[a] For properties inferred from the SED fitting, we quote the median values with uncertainties representing the 16th and 84th percentiles. For further calculations and for the analysis described in the text, we adopt an uncertainty floor of ± 0.3 dex on the values of M_* and SFR (based on the systematic uncertainties).
[b] Calculated based on the Schreiber et al. (2015) best-fit MS. Uncertainties on the MS offset are calculated based on the systematic uncertainties in the SFRs and stellar masses and the uncertainty of the MS function.
[c] CO(1–0)-to-molecular gas conversion calculated based on the metallities inferred via the stellar mass–metallicity relation parameterized in Equation 12(a) of Genzel et al. (2015) and applying Equation (2) of Tacconi et al. (2018).

To estimate the molecular gas masses from our CO observations, we first convert the line fluxes to luminosities (in K km s^{-1} pc^2) following Solomon et al. (1992), via

$$L'_{CO} = 3.25 \times 10^7 S_{CO}\Delta v\ \nu_{obs}^{-2} D_L^2 (1+z)^{-3}, \qquad (1)$$

where $S_{CO}\Delta v$ is the velocity-integrated line flux (in Jy km s^{-1}), ν_{obs} is the observed-frame frequency of the CO transition in GHz, and D_L is the luminosity distance in Mpc. We down-convert these line luminosities to the CO(1–0) line luminosity via the following ratios (Table 2). For ALPS.3, both the CO(3–2) and CO(1–0) transitions have been observed (Riechers et al. 2020). Thus, we apply the measured luminosity ratio $r_{31} = L'_{CO\ (3-2)}/L'_{CO(1-0)} = 0.79 \pm 0.21$. For ALPS.1 and 2, we have no CO(1–0) observations. Thus, we assume an excitation correction based on the measurements of $r_{21} = L'_{CO\ (2-1)}/L'_{CO(1-0)}$ for other high-redshift samples (Bothwell et al. 2013; Spilker et al. 2014; Daddi et al. 2015),

and the values inferred for the ASPECS sample (Boogaard et al. 2020).

To convert the inferred CO(1–0) line luminosities to molecular gas masses we apply CO-to-molecular gas mass conversion factors, α_{CO}, calculated via the assumed metallicities (provided in Table 2). We infer the metallicities (according to the Pettini & Pagel 2004 scale) from the stellar masses using the mass–metallicity calibration in Equation 12(a) of Genzel et al. (2015) (taking into account both the uncertainties on the measured stellar mass and the empirical relation). We note that for ALPS.2 the strong emission lines Hα and [N II] have been observed, yielding a slightly higher inferred metallicity than the value based on the mass–metallicity calibration (Williams et al. 2014). However, the difference is only 0.05 dex, which is lower than the typical systematic uncertainty of metallicity measurements (e.g., Kewley & Ellison 2008). We calculate the CO-to-molecular gas mass conversion factor, α_{CO}, according to Equation (2) of Tacconi et al. (2018). We choose these mass–metallity and α_{CO} calibrations based on the detailed comparison of such relations presented in Appendix A.3 of Liu et al. (2019). The final molecular gas masses quoted in Table 2 are the inferred $L'_{CO(1-0)}$ multiplied by the metallicity-based α_{CO}.

We estimate the total dust masses in two ways; (1) from the spectral energy distribution (SED) fits (see Section 3.2) and (2) from the 1.3 mm (Band 6) flux densities. To convert the flux densities measured at 1.3 mm to dust masses we assume that the dust emission is optically thin and can be modeled by a MBB of the form

$$S_{\nu_{obs}} = (1 + z)D_L^{-2} \kappa_{\nu_{rest}} M_{dust} B_{\nu_{rest}}(T_{dust}), \qquad (2)$$

where $\kappa_{\nu_{rest}}$ is the dust mass opacity coefficient, M_{dust} is the dust mass, $B_{\nu_{rest}}$ is the blackbody radiation spectrum, and T_{dust} is the temperature of the dust. We assume a temperature of 25 K, as motivated in Scoville et al. (2014). We determine the opacity coefficient by relating it to a reference frequency via the power-law dependency

$$\kappa_{\nu_{rest}} = \kappa_{\nu_0}(\nu_{rest}/\nu_0)^{\beta}, \qquad (3)$$

where β is the dust spectral emissivity index. We use the rest frame 850 μm as our reference frequency, taking $\kappa_{\nu_{850\mu m}} = 0.77$ g^{-1} cm^2 (Draine & Lee 1984) and $\beta = 1.8$ (e.g., Planck Collaboration et al. 2011).

For ALPS.1 and 2, the dust masses derived from the 1.3 mm flux densities are larger than the values inferred from the SED fitting (Table 2), although still consistent within errors for ALPS.1. The discrepancy is the result of a combination of the assumed (or fit) temperatures and emissivity indices, which are affected by the active galactic nucleus (AGN) template used for ALPS.2. Unlike the single MBB model, the SED-fitting algorithm MAGPHYS (da Cunha et al. 2008, 2015) includes both a warm and cold dust component with emissivity indices of 1.5 and 2, respectively. The temperature of the two components is determined during the fit. Thus, the mass-weighted temperature is not fixed. For ALPS.2 in particular, the mass-weighted temperature of the MAGPHYS fit is greater than for the single MBB, resulting in the difference between the two values.

3.2. Stellar Masses and SFRs

We rely on SED modeling to infer the stellar masses and SFRs of our sources. As part of the HUDF, our sample has been observed with a wide range of ground- and space-based observatories. To trace the extent of the stellar continuum, we rely on the HST/WFC3 F160W images from the eXtreme Deep Field (XDF) data release, described in Illingworth et al. (2013).[19] Given our small sample size and use of the HST/WFC3 F160W Band to trace the stellar continuum, we revisit the accuracy of the HST photometry in Appendix B.

We select the following sets of data for the SED analysis. For the UV-NIR photometry we use the values from the Guo et al. (2013) catalog, which are extracted from large enough apertures to enclose the full extent of the emission for the extended sources analyzed here (see Appendix B). In addition, we use the deblended Spitzer/MIPS 24 μm photometry from Whitaker et al. (2014) and the deblended Herschel/PACS 100 and 160 μm data from Elbaz et al. (2011). We take the maximum of the local and simulated noise levels as the uncertainties for the Herschel data. We also use the 1.3 mm dust-continuum measurements of Dunlop et al. (2017) and González-López et al. (2019) and the 3 mm continuum limits presented in González-López et al. (2019).

We model the photometry using two adapted versions of the high-redshift extension to the SED-fitting algorithm MAGPHYS (da Cunha et al. 2008, 2015). To account for the impact of obscuration and high SFRs on the attenuation, we apply the adaptation to the high-redshift extension of the MAGPHYS code, developed by Battisti et al. (2019). We find that this adapted version significantly reduces the fitting residuals, particularly for ALPS.3 (see Appendix B). Thus, we quote the fitting parameters from this adaptation of MAGPHYS for ALPS.1 and 3 in Table 2. Despite the more sophisticated dust treatment, the Infrared Array Camera (IRAC) and Photodetector Array Camera (PACS) photometry for ALPS.2 remain poorly fitted by the adapted version of MAGPHYS. This is likely because of the presence of an AGN, identified from Chandra observations (the details of which are described in Luo et al. 2017). Thus, for ALPS.2 we apply the adapted version of MAGPHYS that accounts for a contribution by an AGN to the dust heating (Chang et al. 2020). The inferred stellar mass and SFR are a factor of 2 and 1.6 times smaller, respectively, when the AGN component is considered. We note that this extension does not include the adaptations introduced by Battisti et al. (2019). We provide the parameters from the fit, including ξ_{AGN}, the estimated fraction of the template AGN emission contributing to the total IR luminosity, in Table 2. Based on the variation in the derived stellar masses and SFRs for different sets of photometry, the inclusion/exclusion of an AGN component, and the choice of applied dust attentuation curve, we adopt an uncertainty floor on the stellar masses and SFRs of $\pm\sim0.3$ dex, consistent with a factor of ~2 increase/decrease in stellar mass and factor of ~1.5 increase/decrease in SFR. We show the photometry and best-fit SED models for the three galaxies in Figure 3.

To place our sources in the context of the MS, at the measured redshift of each source, we apply the best-fit MS relation of Schreiber et al. (2015). We choose this MS for consistency with the HUDF and ASPECS parent samples shown in Aravena et al. (2020) (see their Figure 6), which we also compare to in Figure 1. We note that the exact shape of the MS, particularly for the large stellar masses of our three galaxies, is still under debate (the functional forms of, e.g.,

---

[19] https://archive.stsci.edu/prepds/xdf/

Table 3
H$_2$ Mass and Column Sensitivities

Source	ALPS.1	ALPS.2	ALPS.3
rms values of the ...			
1.3 mm map (μJy)	15	18	14
CO moment-0 map (mJy km s^{-1})	49	20	25
H$_2$ mass limit per beam ($10^8 M_\odot$ beam^{-1})			
Dust-based[a]	28 $\pm$ 14	34 $\pm$ 17	24 $\pm$ 12
CO-based[b]	55 $\pm$ 6	28 $\pm$ 3	48 $\pm$ 5
H$_2$ column density limit per beam (10^{21} cm^{-2} beam^{-1})[c]			
Dust-based	2.7 $\pm$ 1.4	4.6 $\pm$ 2.3	2.9 $\pm$ 1.4
CO-based	5.3 $\pm$ 0.5	3.9 $\pm$ 0.4	5.7 $\pm$ 0.6

Notes. The sensitivity estimates are based on 1σ (i.e., applying the rms values at the top of the table).
[a] Calculated assuming a gas-to-dust mass ratio of 200 $\pm$ 100, with the dust emission described by an MBB with $T = 25$ K, $\beta = 1.8$.
[b] Calculated based on the α_{CO} in Table 2.
[c] Calculated using the CO beam size in Table 1.

Whitaker et al. 2012, 2014; Speagle et al. 2014; Schreiber et al. 2015; Boogaard et al. 2018; Leslie et al. 2020, differ). Our sources range from having specific SFRs (sSFR = SFR/M_*) consistent with the MS to being slightly below the MS, with specific star formation rates relative to the MS of sSFR/sSFR$_{MS}$ = 0.2–0.4, based on the Schreiber et al. (2015) MS. This places our three galaxies in a regime that has been scarcely sampled to date (e.g., Bolatto et al. 2015 have resolved CO observations for two MS sources at $z \sim 2$). Moreover, based on the derived flux densities, our sources appear to have large gas mass fractions $M_{mol}/M_* = 0.4$–0.8 and gas-to-dust ratios (GDRs) typical of MS galaxies and SMGs, i.e., $M_{mol}/M_{dust} \sim 100$–300. (For this comparison, we use the dust mass inferred from the 1.3 mm continuum.)

4. Galaxy Size Analysis

4.1. Sensitivity Comparison

Before comparing the spatial distribution of the dust-continuum and CO emission, we investigate how sensitive our ALMA data are to to the molecular gas. We estimate the minimum H$_2$ mass and column densities that are observable based on our 1.3 mm continuum and CO moment-0 maps, comparing values at a matched resolution given by the CO moment-0 map beam size. To estimate the CO-based H$_2$ mass limit per beam, we take the rms of the moment-0 maps and scale to a line luminosity limit using the α_{CO} conversion factors in Table 2. We account for the solid angle of the beam to derive the column density limit. For the dust-based values, we take the rms of the dust-continuum maps and scale these values to the beam size of the CO moment-0 maps. We convert the rms per beam to an inferred H$_2$ mass per beam by assuming a MBB with the same assumptions on the temperature, emissivity index, and opacity described in Section 3.1. We apply a GDR of 200 $\pm$ 100, consistent with what we measure for our sample (Table 2). Based on these assumptions, we derive the sensitivities in Table 3. Note that here we compare the values for H$_2$ only, whereas we consider the total molecular gas masses (which include He) in the rest of the text.
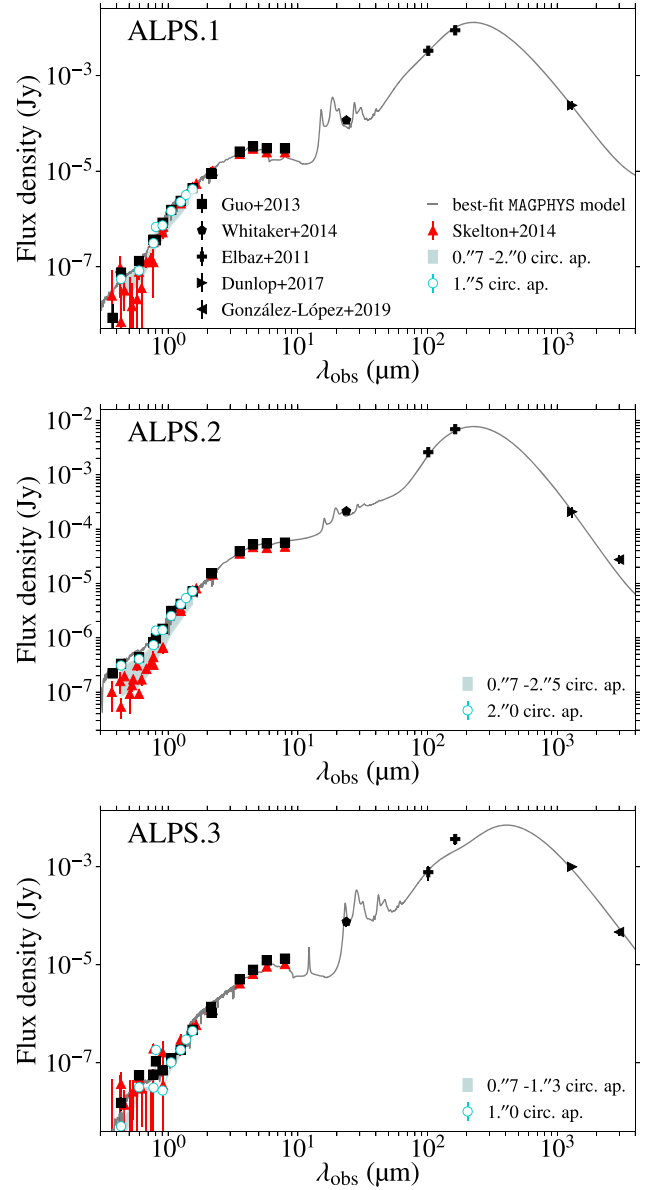
Figure 3. Photometry used for the SED modeling (black filled symbols) and best-fit solutions (black lines) for our three sources. The UV-IR photometry of Guo et al. (2013) (black squares) and Skelton et al. (2014) (red triangles) are also compared (see Appendix B). Compared with the Skelton et al. (2014) photometry, we find the Guo et al. (2013) HST photometry to be systematically larger for the measurements from the rest-frame UV-optical (particularly at 1.6 μm), consistent with what we measure from apertures enclosing the extent of the source emission (cyan circles representing the flux measured from the XDF images within circular apertures encompassing the full extent of source emission). This is especially true for the most extended source, ALPS.2. Also shown are the Spitzer, Herschel, and ALMA continuum data used to constrain the SEDs (as described in the legend).

The sensitivities calculated here, multiplied by a suitable S/N, represent the minimum observable column density assuming that the total area of the beam is covered by source emission (i.e., a beam filling factor of unity). In the case of a spiral arm, the actual CO column would fill only a fraction of the beam, e.g., if a spiral arm covers only a tenth of the beam area, then the actual column density of molecular gas that our data are sensitive to is 10 times what is quoted here. To detect the molecular gas at 3σ, the column densities would have to be $\sim 10^{22}$ cm^{-2} (modulo the beam filling factor). For local disks,
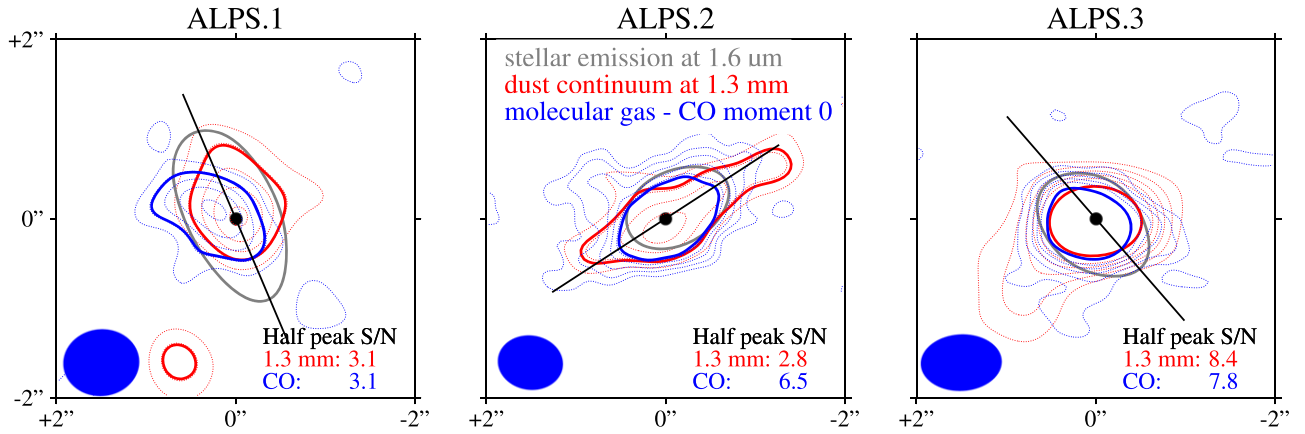
Figure 4. Comparison of the half-peak emission contours (solid lines) for the stellar emission at 1.6 μm (gray), the 1.3 mm dust-continuum emission (red), and the CO line emission (blue), which probes the molecular gas. Both the 1.3 mm dust continuum and HST F160W maps have been convolved to the resolution of the CO emission. Each panel shows a different source, labeled at the top. The dotted contours depict the CO (blue) and convolved 1.3 mm continuum (red) data, starting at $+2\sigma$ and increasing in steps of $+1\sigma$. The ratio of the half-peak value to the rms (half-peak S/N) for both the 1.3 mm and CO data are listed on the bottom right of each panel. The black filled circle and line represent the kinematic center and position angle used to extract the major axis profiles in the next figure. The HST astrometry has been corrected according to the offsets measured by Franco et al. (2020).

the typical column densities of the bar and spiral arms are 10^{21}–10^{22} cm^{-2}, whereas the column densities measured for the central starbursts are up to an order of magnitude higher, e.g., the column density of the nuclear region of NGC 253 is $2 \times 10^{23} \times$ cm^{-2} (Weiß et al. 2008). This difference in column densities leads to a significant contrast between the nuclear region and the brightest parts of the disks (and bar), i.e., factor of 20–50× in the observed flux densities.

Based on the estimated sensitivities, our CO and dust-continuum observations appear to be sensitive to approximately the same column of molecular gas. The values estimated for the CO and continuum data are consistent within the uncertainties (based on the above assumptions) for ALPS.1 and 2, whereas for ALPS.3 the dust continuum may be marginally (up to 20%) more sensitive to the H$_2$ column. Comparing the CO data across our sample, the sensitivity is highest for ALPS.2. However, the continuum data of our sample have similar sensitivities, with slightly lower inferred H$_2$ mass and column density limits per beam for ALPS.1 and 3 versus ALPS.2. The comparison between CO and dust-based H$_2$ column sensitivities is based on the assumptions that the dust temperature and GDR remain constant across the disk. Variations in the temperature or GDR would serve to decrease the sensitivities of the dust emission, compared with CO, at larger radii.

4.2. Qualitative Comparison of Spatial Extents

Our aim is to quantify the sizes of the rest-frame optical, CO, and dust-continuum emission. However, to aid the interpretation of our data, we begin with a qualitative comparison. In Figure 4, we compare the observed galaxy extents at half the peak surface brightness (solid lines) of the rest-frame optical, dust-continuum, and CO emission (with both the F160W and Band 6 dust continuum convolved to the resolution of the CO moment-0 maps). The F160W maps have been corrected for the offset of the HST astrometry measured by Franco et al. (2020) (for which the median offset is −96 mas in R.A. and +261 mas in decl. and the additional local offsets for our sources differ from the medians by ⩽40 mas). We list the S/N at half the peak surface brightness for the CO and 1.3 mm continuum in the bottom right corner of each panel. For ALPS.1, the CO and 1.3 mm continuum half-peak values are barely greater than 3σ. For ALPS.2, the half-peak value of the

1.3 mm emission is below 3σ. In contrast, for the 1.6 μm data, the S/N at half the peak value is at >50 for each source.
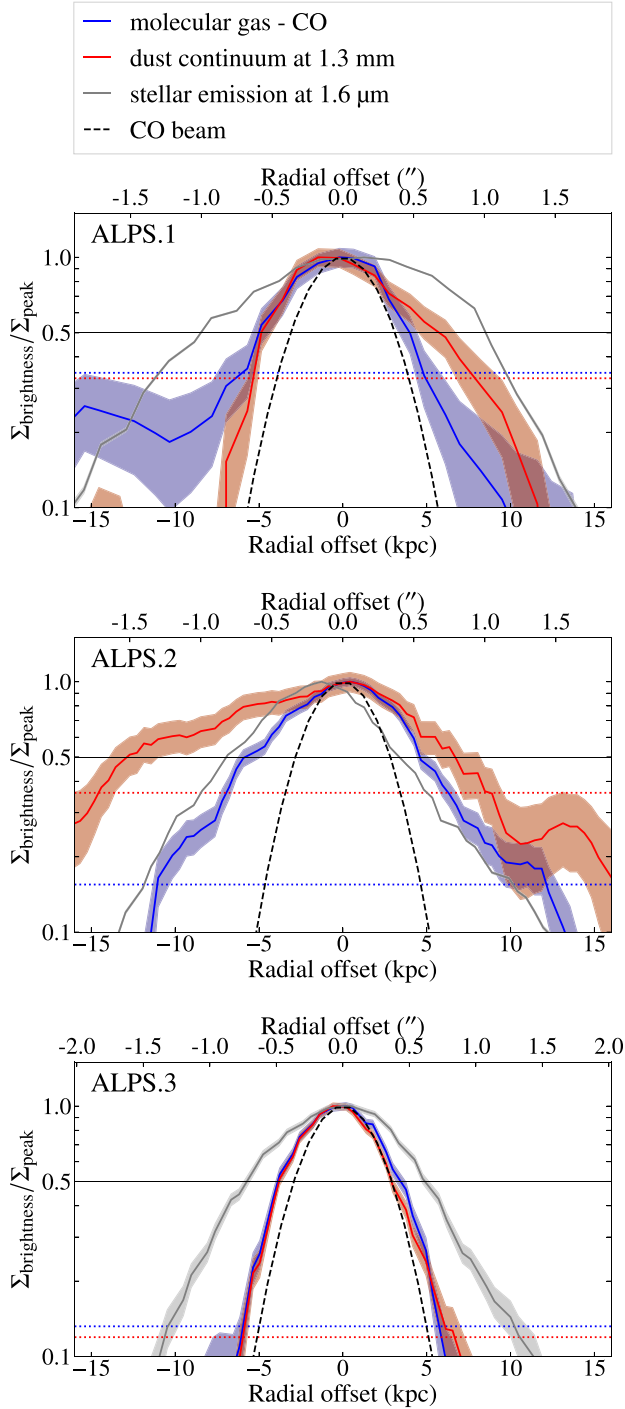
We compare the normalized surface brightness profiles extracted along the entire major axis (see Figure 5). The normalized major axis cut illustrates how the steepness of the surface brightness profiles compare and indicates a potential difference in the peak positions (for the three types of emissions). We show the beam-convolved major axis profiles because the accurate construction and interpretation of the radial profiles for the CO and 1.3 mm continuum emission were hindered by the poor S/N and resolution. To indicate how well our data are resolved, we compare the CO beam (dashed black lines) with the major axis profiles and show the 2σ level normalized to the peak flux of the CO and 1.3 mm continuum emission (dotted blue and red lines).

From Figures 4 and 5 it appears that for ALPS.1, little CO or dust-continuum emission is recovered, at >2σ, on scales greater than the beam size. For ALPS.2, a significant fraction of CO and dust-continuum emission appears to be on scales larger than the beam size. In contrast, for ALPS.3, the dust and CO emission are centrally concentrated, with scarcely any emission apparent on scales greater than the image resolution. We quantify the fraction of flux within the beam area (i.e., consistent with a point source) in Section 4.3. The stellar-continuum emission from ALPS.1 and 3 appears to stem from a significantly larger region than the CO or dust continuum. However, for ALPS.2, the stellar emission follows a similar profile to the CO emission, with the dust continuum exhibiting a flatter, extended profile, albeit at a S/N < 3.

4.3. Measuring Galaxy Sizes

To quantify the source sizes, we attempt various fitting methods. For the interferometric data (i.e., the CO and dust-continuum data) there are two possible approaches; fitting the maps (i.e., the image plane), or directly fitting the visibilities (i.e., the uv-plane). For both approaches we use the axis ratios and position angles determined by van der Wel et al. (2012) from the F160W images and provided in Table 4, as initial estimates.

— molecular gas - CO
— dust continuum at 1.3 mm
— stellar emission at 1.6 μm
--- CO beam

Figure 5. Comparison of the normalized surface brightness profiles ($\Sigma_{\mathrm{brightness}}/\Sigma_{\mathrm{peak}}$) of stellar emission from the F160W image (gray), 1.3 mm dust continuum (red), and CO emission, from the moment-0 map (blue) along the major axes of each source (labeled at top left of each panel). The horizontal black line of each panel indicates half the maximum surface brightness, thereby allowing the FWHM of the three profiles to be compared. The 2σ levels relative to the peak surface brightness of the CO and dust-continuum emission are indicated by the blue and red dotted lines, respectively. The major axes, from which these profiles are extracted, are shown in Figure 4. The HST astrometry has been corrected according to the astrometric offsets provided by Franco et al. (2020).

4.3.1. Image-plane Analysis

Before performing the image-plane analysis, we check whether our ALMA data have sufficient sensitivity and spatial

Table 4
Inferred Source Sizes

| Source	ALPS.1	ALPS.2	ALPS.3
Structural parameters from van der Wel et al. (2012) [a]			
$r_{1/2}^{\mathrm{F160W}}$ (kpc)	7.46 ± 0.02	8.28 ± 0.03	4.84 ± 0.15
Sérsic index	0.48 ± 0.00	3.04 ± 0.02	0.86 ± 0.06
Position angle (degrees)	23.2 ± 0.1	302.5 ± 0.1	220.9 ± 1.1
Axis ratio	0.247 ± 0.002	0.452 ± 0.002	0.458 ± 0.013
Half-light radii measured here using GALFIT [b]			
$r_{1/2}^{\mathrm{F160W}}$ (kpc)	7.9 ± 0.8	8.0 ± 0.8	4.9 ± 0.5
Sérsic index (F160W)	0.6 ± 0.1	2.1 ± 0.2	0.7 ± 0.1
$r_{1/2}^{\mathrm{CO}}$ (kpc)	5.8 ± 1.7	5.5 ± 0.8	<3.4
$r_{1/2}^{\mathrm{dust}}$ (kpc)	3.9 ± 1.2	9.4 ± 1.4	<1.2

Notes.
[a] Used as priors for the GALFIT fitting.
[b] Measurements based on an exponential surface brightness profile.

resolution to estimate source sizes. To this end, we fit the emission of each source with a model point source. We check the residuals of the image-plane fit (subtracting the beam-convolved point source model from the image) and compare the point source fluxes to the measured flux densities. For ALPS.1 and 2 we recover remaining, residual structure (at $>2\sigma$) and find that the flux densities of the point source fits are $40 \pm 20\%$ lower than our measured values. Conversely, for ALPS.3, we recover no significant residual CO or continuum emission at a spatial scale greater than that of the synthesized beams and find that the flux densities of the point source models are consistent with the measured values. Thus, for ALPS.3, we place 2σ upper limits on the half-light radii that can be measured from the moment-0 CO and dust-continuum maps. Because the emission of ALPS.3 is indistinguishable from the beam, we quantify the 2σ upper limit based on the convolution of two Gaussian profiles, via

$$\mathrm{FWHM}_{\mathrm{true}}^2 < (\mathrm{FWHM}_{\mathrm{beam}} + 2\delta\mathrm{FWHM}_{\mathrm{obs}})^2 - \mathrm{FWHM}_{\mathrm{beam}}^2, \tag{4}$$

where $\mathrm{FWHM}_{\mathrm{true}}$ is the intrinsic FWHM of the galaxy, assuming a Gaussian profile, and $\delta\mathrm{FWHM}_{\mathrm{obs}}$ is the error on measuring the FWHM based on the rms of the map. The values are given in Table 4. Although ALPS.3 is not sufficiently resolved in the CO moment-0 map, the 3D data indicate that ALPS.3 is marginally resolved, with the location of the emission shifting for different velocity channels (as indicated by the position–velocity diagram in Figure 6).

Having established that the CO line and 1.3 mm continuum emission of ALPS.1 and 2 are sufficiently resolved, we attempt to quantify the potential asymmetries visible in Figures 4 and 5. Following the second equation of Section 3.2 in Conselice et al. (2000), we calculate the asymmetry parameter (see also Conselice 2003). Note that a value of 0 corresponds to a galaxy that is perfectly symmetric, whereas a value of 1 indicates that a galaxy is completely asymmetric. For ALPS.1, we derive asymmetry parameters of $A = 0.5 \pm 0.2$ and $A = 0.7 \pm 0.1$ for the CO and 1.3 mm continuum emissions, respectively. Similarly, for ALPS.2, we derive asymmetry parameters of $A = 0.6 \pm 0.1$ and $A = 0.7 \pm 0.1$ for the CO
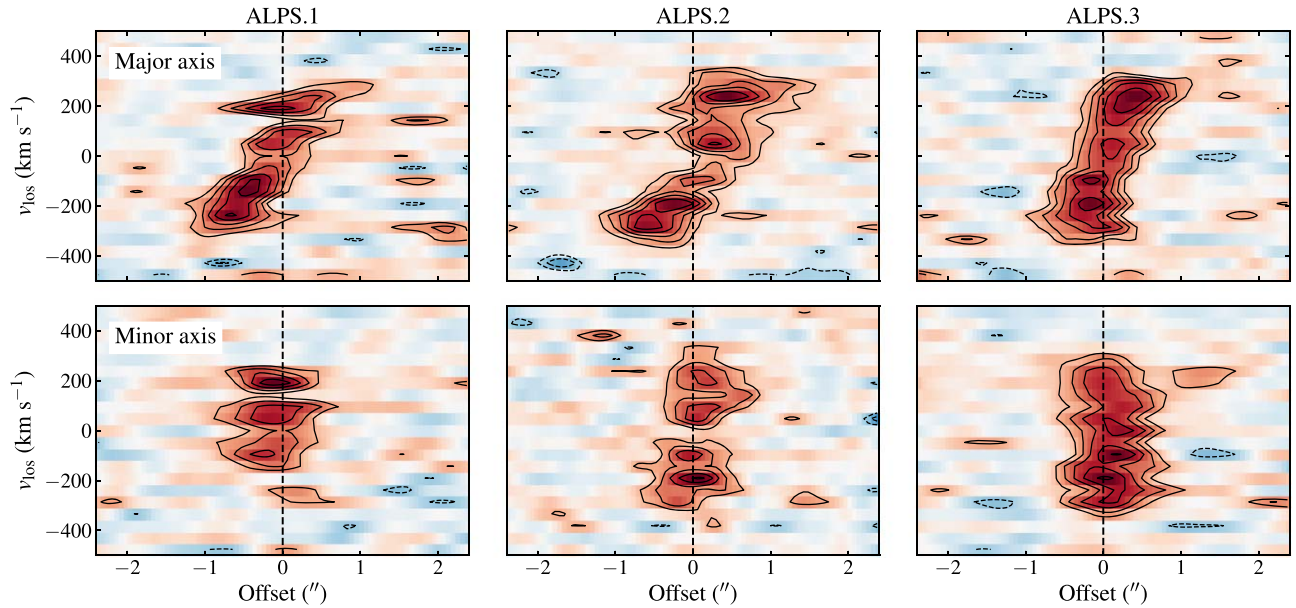
Figure 6. Position–Velocity (pV) diagrams extracted over ± 500 km s^{-1} within 0$\farcs$3 wide slits along the rotation axis (where the position angle is taken from the kinematic modeling of the CO data, described in Section 5.2) using CASA's impv. Top row: position–velocity (pV) diagram along major axis. We see clear evidence of rotation in all three galaxies. Bottom row: pV diagram along minor axis. The flux density is represented by the linear, blue-to-red color scale, in which white represents the zero level. Contours start at $\pm 2\sigma$ and proceed in steps of $\pm 1\sigma$.

and 1.3 mm continuum emission. Although this indicates that the observed emission is somewhat asymmetric, for both types of emissions, we note that the exact noise structure and resolution heavily bias these values in ways that are challenging to quantify. Nonetheless, the values calculated here indicate that the surface brightness profiles are not well described by symmetric 2D profiles.

Despite these potential asymmetries, we estimate the stellar, dust, and CO half-light radii by fitting the respective maps with 2D surface brightness profiles via GALFIT (Peng et al. 2002, 2010). For each source of emission (stellar, dust, and CO), we fit a 4″ region centered on the source. We consider uniform error maps, with a constant background noise given by the rms of the full image. For the input point-spread functions (PSFs), we supply images of 2D Gaussian profiles according to the HST PSF size and major and minor FWHM of the synthesized beam (of the ALMA data). We allow the position and inclination angles of the best-fit models to be within $\pm 10°$ of the best-fit values from van der Wel et al. (2012) and constrain the source centers to vary by $\pm 0\farcs2$ of the centers estimated by van der Wel et al. (2012).

We perform multiple tests to check to what extent we can recover the source sizes and Sérsic profile shapes for different intrinsic sizes, profile shapes, and peak signal-to-noise values. Based on sets of simulated data at the resolution and S/N of the observations, we find that we can accurately constrain the Sérsic index, n, of the 1.6 μm surface brightness profiles. For all three galaxies, exponential profiles ($n = 1$) provide a poor fit to the 1.6 μm emission (see also Calistro Rivera et al. 2018). In contrast to the 1.6 μm emission, the Sérsic indices cannot be accurately constrained for the dust and CO emission (based on the S/N and resolution). We therefore keep the Sérsic index as a free parameter when fitting the F160W emission but fix the Sérsic index to match an exponential profile ($n = 1$) for the CO and dust emission. This choice of exponential profile is motivated by the exponential dust-continuum profiles observed

for local (e.g., Haas et al. 1998; Bianchi 2007; Muñoz-Mateos et al. 2009; Bianchi & Xilouris 2011) and high-redshift galaxies (Barro et al. 2016; Hodge et al. 2016; Tadaki et al. 2017a; Calistro Rivera et al. 2018; Gullberg et al. 2019). Fixing the profile shape for the CO and dust continuum has negligible impact on our conclusions because the half-light radii inferred when forcing $n = 1$ are consistent, within errors, with the values inferred when n is a free parameter. The same is not true if we fix the 1.6 μm emission to be exponential. In that case, the half-light radii measured for ALPS.1 and 2 are 20% larger and 30% smaller respectively, thanks to the presence of multiple, unobscured, stellar components, visible in the 1.6 μm emission, as well as possible contributions from dust lanes.

The uncertainties returned by GALFIT, based on the uniform error maps, underestimate the uncertainty on the fit parameters. We therefore quote uncertainties based on the distribution of best-fit values for fits to simulated maps. For the F160W emission, the error on the measured half-light radii is $\leqslant 10\%$, whereas for the CO and dust-continuum emission the uncertainties (not accounting for the uncertainty of the profile shape) are $\sim 20\%$–30%.

The F160W half-light radii measured here are consistent with those of van der Wel et al. (2012). The small differences in the best-fit values appear to be because of the deeper XDF data of Illingworth et al. (2013) used here. The steepness of the stellar surface brightness profiles differs significantly for the three sources. ALPS.1 exhibits the steepest surface brightness profile, with a Sérsic index of $n \sim 0.5$, equivalent to a Gaussian profile. The unobscured stellar emission of ALPS.3 is best fit by $n \sim 0.8$ (close to the exponential profile, $n = 1$), whereas ALPS.2 exhibits the shallowest, unobscured stellar profile with $n > 2$. We note that of the sources at $1 < z < 3$ in the GOODS-South field with measured structural properties, a third have profiles with $n > 2$, whereas 12% are best fit by Sérsic indices $n \lesssim 0.5$.
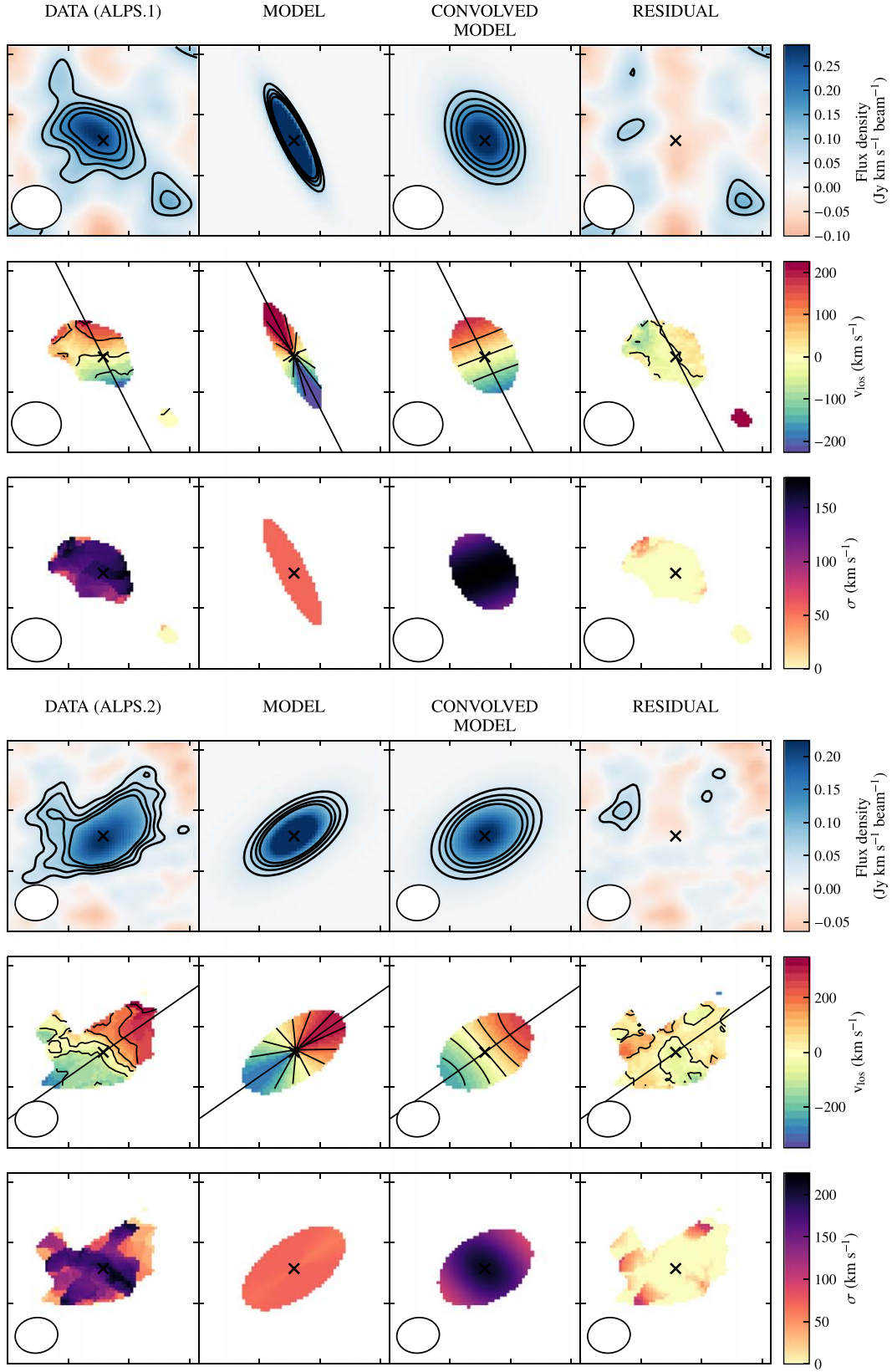
Figure 7. QUBEFIT models of the integrated CO flux (top row), velocity (middle row), and velocity dispersion (bottom row) of ALPS.1, 2, and 3 (labeled above data column for each). For ALPS.1 and 2 we observe CO(2–1), whereas for ALPS.3 we observe CO(3–2). From left to right: data, intrinsic model, convolved model, and residual (data—convolved model). The maps of the integrated velocity and velocity dispersion have been created using the 2σ blanking method (described in Section 5.2). For clarity, the maps are additionally masked at the outer 2σ contour of the integrated intensity (top row) for the respective column (data, model, and convolved model). The best-fit position angles are indicated by the black lines.
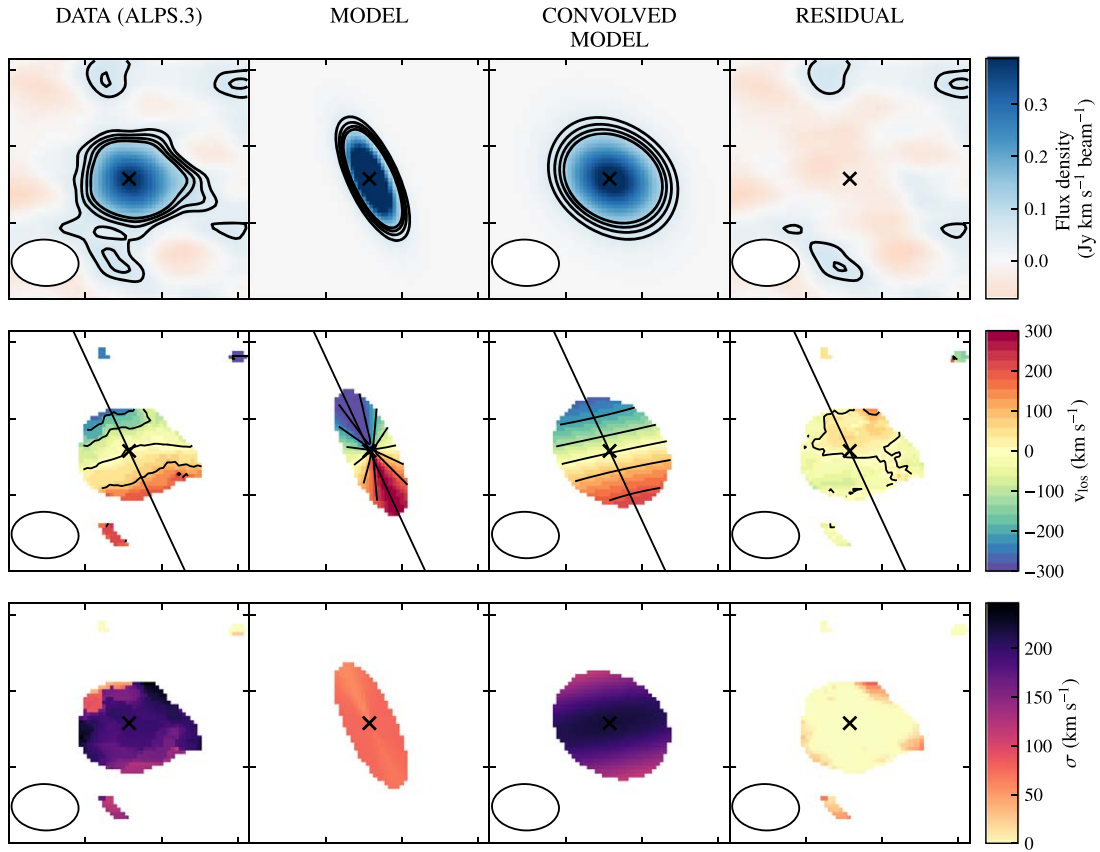
Figure 7. (Continued.)

4.3.2. Uv-plane Analysis

To assess the reliability of our image-plane analysis, we also perform *uv*-plane source fitting using: (1) the CASA-based UVMULTIFIT algorithm (Martí-Vidal et al. 2014), and (2) the GILDAS-based[20] UV_FIT algorithm (Pety 2005). Both algorithms fit the specified Fourier-transformed 2D surface brightness profiles, i.e., the model visibilities, to the measured visibilities by minimizing the χ^2 statistic. We correct for the fact that our sources are not at the center of the pointings by applying the necessary phase shifts, baseline reprojections, and primary beam corrections. These corrections are applied as part of the UVMULTIFIT algorithm, whereas for the second approach, we corrected for the primary beam attenuation and weighting using GILDAS algorithms before merging the visibilities from the various mosaic pointings for each source. We fit both 2D elliptic Gaussian and exponential profiles but find no significant differences ($<5\%$ in the flux and $<25\%$ in size) between the two profiles. We refer to the exponential fits from hereon for consistency with the image-plane analysis. Additional uncertainties are introduced by the relative weighting of the low- versus high-resolution data sets, with differences of up to 40% in the inferred sizes (i.e., comparing the fits using both data sets versus the high-resolution set only).

For all three sources, we find good agreement between the fluxes fit in the *uv*-plane and those measured from the image plane (as described in Section 3.1). Without fixing any parameters, we find that the *uv*-based CO- and 1.3 mm size

estimates for ALPS.1 and 3 are consistent, within 1σ errors, with the measurements and upper limits from the image plane, whereas for ALPS.2 (owing to the low S/N and the apparently complex morphology), the sizes fit in the *uv*-plane are $50 \pm 30\%$ smaller than those fit in the image plane. However, when we fix the source center and position angle to the results of our CO kinematic fitting (described in Section 5.2) during the *uv* fitting, we obtain half-light radii that are consistent with what we measure from the image plane. Although 20% smaller on average, we conclude that our *uv*- and image-plane analyses are consistent within errors for all three sources, when the source centers and position angles are fixed. Henceforth, we quote the image-plane sizes.

5. Dynamical Analysis

5.1. CO Line Kinematics

To understand the dynamical properties of our sources, we first analyze their position–velocity (pV) diagrams, shown in Figure 6. We create the pV maps from the 50 km s^{-1}, CO cubes using CASA's IMPV task, selecting a 0″3 slit along the major axis, which we define using the centers and position angles fit to the CO data (see Section 5.2). We find clear velocity gradients for all three sources (also evident from the moment-1 maps in Figure 7), suggesting that the bulk of the emission stems from rotation-dominated gas disks. The maximum line-of-sight velocities are $\sim$300 km s^{-1}, indicating rotation velocities of 310–340 km s^{-1} (based on the inclinations inferred from the HST data).
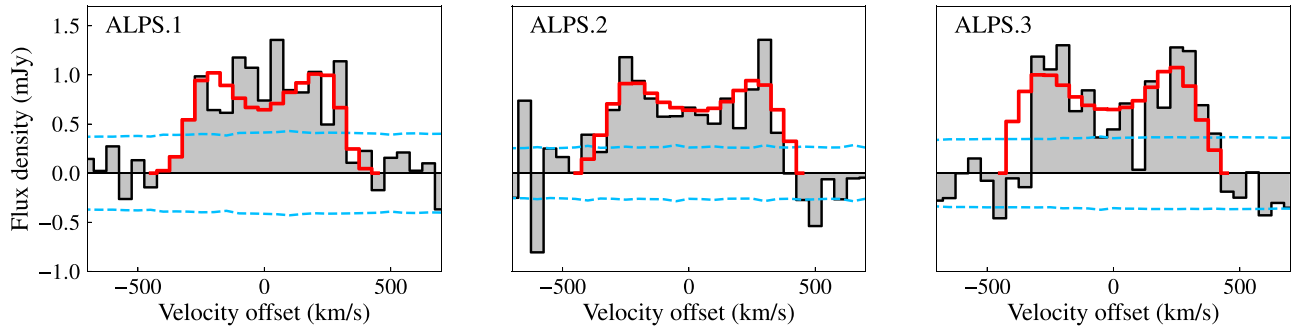
Figure 8. CO spectra of our sources, taken from within 1″5, 2″, and 1″5 apertures respectively for ALPS.1, 2, and 3. We compare the line profiles from the 3D convolved model of the CO emission, fit using qubefit (in red). The $\pm\sigma$ levels are indicated by the light blue, dashed lines. All line profiles are inconsistent with a single Gaussian profile. The profiles for ALPS.2 and 3 are clearly double-horned, indicating that the CO emission stems from rotation-dominated disks.

We also assess the integrated CO spectra of our sample. The spectra from the ASPECS LP data are shown in Figure 2 of Aravena et al. (2019) and Figure 8 of González-López et al. (2019). We also provide the spectra of our three sources, based on the combined ASPECS LP and ALPS data, in Figure 8, comparing the line profile predicted from the dynamical modeling (described in Section 5.2). The observed shape of the line profile is governed by multiple effects, including the inclination, velocity dispersion, total mass (related to the stellar and gas mass distributions), and steepness of the gas surface density profile (de Blok and Walter 2014). Distinct, double-horned profiles originate from gas that is supported by rotation in a disk, and for which the rotation velocity increases sharply at small radii and flattens at larger radii. ALPS.2 and 3 both display double-horned profiles, indicating that the emission from each source stems from a rotation-dominated disk. Such profiles are commonly observed for local disk galaxies using H I, which traces the gas disk to large radii (e.g., Catinella et al. 2010).

About half of the SMGs observed at sufficient S/N exhibit double-peaked lines profiles (e.g., J. Birkin et al. 2020, in preparation). Double-horned profiles are more commonly observed for massive star-forming galaxies with extended molecular gas disks (such as our sample) (e.g., Tacconi et al. 2013). The flatter-than-Gaussian profiles observed for some high-redshift galaxies are sometimes interpreted as further evidence that the gas is more turbulent than in local galaxies. However, for many observed sources it is also possible that the observed emission stems from a small, central region that does not probe the maximum rotation velocity (i.e., where the velocity curve flattens). Although we infer the velocity dispersions and maximum rotation velocities in the next section, we note here that the flat CO line profile of ALPS.1, compared with the separate peaks observed for ALPS.2 and 3, may be the result of a steeper surface density profile (i.e., as indicated by the smaller Sérsic index of the fit to the stellar emission) or the fact that the CO observations, for this source, are less sensitive to the flat part of the rotation curve.

5.2. Kinematic Modeling

We constrain the rotation velocity and velocity dispersion of each of the three galaxies using the python-based kinematic modeling tool QUBEFIT, (described in Appendix C. of Neeleman et al. 2019).[21] QUBEFIT fits a model cube to the data, convolving the model to the same spectral and spatial resolution as the data. The model is compared with the data via the χ^2 statistic,

---
[21] https://github.com/mneeleman/qubefit

Table 5
Inferred Dynamical Properties

Source	ALPS.1	ALPS.2	ALPS.3
Kinematic Analysis with QUBEFIT			
Inclination (degrees)	76^{+10}_{-4}	60^{+4}_{-4}	69^{+6}_{-6}
$r_{1/2}^{CO}$ (kpc)	$3.7^{+0.3}_{-0.3}$	$4.6^{+0.3}_{-0.3}$	$2.6^{+0.2}_{-0.3}$
$v_{rot,max}$ (km s^{-1})	279^{+8}_{-14}	355^{+12}_{-14}	349^{+19}_{-23}
σ (km s^{-1})	57^{+11}_{-12}	73^{+13}_{-14}	77^{+10}_{-11}
$v_{rot,max}/\sigma$	4.9 ± 1.0	4.9 ± 0.9	4.5 ± 0.7
Dynamical analysis within $2\,r_{1/2}^{CO}$			
M_{dyn} ($10^{11}\,M_\odot$)	1.3 ± 0.2	2.7 ± 0.3	1.5 ± 0.2
M_{baryon} ($10^{11}\,M_\odot$)	1.9 ± 0.7	1.3 ± 0.6	2.4 ± 0.9
f_{DM}	>0.3	0.5 ± 0.2	>0.4
Dynamical analysis within $6\,r_d^{CO}$			
M_{dyn} ($10^{11}\,M_\odot$)	2.4 ± 0.3	4.8 ± 0.5	2.6 ± 0.4
M_{baryon} ($10^{11}\,M_\odot$)	2.6 ± 1.0	1.7 ± 0.9	3.6 ± 1.3
f_{DM}	<0.2	0.6 ± 0.2	>0.3

Note. The baryonic masses and hence dark matter fractions depend on the inferred α_{CO}, provided in Table 2. The quoted uncertainties are at the 1σ level, whereas the upper limits are at 2σ.

and takes into account the spatial correlation between pixels via a bootstrapping analysis. The full parameter space is sampled via the Markov Chain Monte Carlo method, thereby yielding likelihood distributions for the parameters being fit.

We model the line emission as stemming from a thin, exponential disk with only circular velocities in the plane of the disk, i.e., we do not consider any radial motions. We fit for the source center, maximum rotational velocity, $v_{rot,max}$, velocity dispersion, σ_v and the scale length of the exponential disk, r_d. The median and $\pm 1\sigma$ values for each galaxy are provided in Table 5. We choose not to place a prior on the inclination or PA because the CO emission may probe a different region than the rest-frame optical data. For the initial guesses of the inclination and position angle, we use the best-fit values of van der Wel et al. (2012), scaling the best-fit axis ratio, q, to an inclination via $\cos^2 i = q^2$. We fit the model cube to regions of 3″ diameter (larger regions resulted in poorer constraints). We note that the best-fit rotation velocities and inclination angles are highly degenerate. However, for all three galaxies we recover inclination angles consistent with those inferred based on the axis ratios fit to the HST data. For ALPS.3, the best-fit position angle differs by 20° from the position angle fit to the HST data. Forcing the position angle to match decreases the rotation velocity to a value 20 km s^{-1} lower

than that quoted in Table 5. We caution that the inferred velocity dispersions are global estimates that include dispersions due to motion along the line of sight (i.e., due to motion inside a thick disk, or motions due to warps), as well the true velocity dispersion of the gas. Thus, the dispersion inferred via QUBEFIT is an upper limit on the intrinsic gas velocity dispersion. Although we provide the estimated errors for the thin disk model in Table 5, we treat the dispersion values as upper limits. The CO half-light radii measured with QUBEFIT are lower than measured from the moment-0 maps with GALFIT, by at least 20%. We conclude that this is mainly due to the low S/N of the emission in individual 50 km s^{-1} channels compared with that in the map collapsed over 800 km s^{-1}.

We compare the model moment maps to those of the data in Figure 7. To create the moment-1 and 2 maps for the data, we implement a PYTHON-based algorithm that identifies coherent source emission, associated with a $>3\sigma$ peak in both the spatial and spectral axis (see also Leroy et al. 2009). To do this, we expand the region around each $>3\sigma$ peak outwards, in R.A., decl., and velocity, until we reach a 2σ boundary. All pixels outside these boundaries are masked when making the moment-1 (intensity-weighted velocity) and moment-2 (intensity-weighted velocity dispersion) maps. This method produces moment maps that are more representative of the velocity fields than if we include all pixels, but some artifacts, such as the 400 km s^{-1} components for ALPS.3, still remain. The residuals of the moment 0–2 maps indicate a good quality of fit (see Figure 7), and the rotation velocity and dispersion values are consistent with the best-fit parameters inferred using the 3D modeling algorithm 3DBAROLO (Di Teodoro & Fraternali 2015). However, for any fitting method the degeneracy between the rotation velocity and inclination is large.

Based on the data presented here, we note that single Gaussian line profiles can severely overestimate the disk rotation. From the single Gaussian fit to the CO spectrum (of the ASPECS LP data), presented in González-López et al. (2019), the FWHM of the CO(2–1) line for ALPS.2 (ASPECS LP 3 mm.05) is FWHM $= 620 \pm 60$ km s^{-1}. If the gas exhibits ordered motion, then the maximum rotation velocity can be approximated by $v_{rot} = 0.75$ FWHM$/\sin i$ (see, e.g., Wang et al. 2013; Willott et al. 2015; Decarli et al. 2018). For ALPS.2, this results in an estimated rotation velocity of $\sim510 \pm 50$ km s^{-1}, significantly larger than the value measured from the 3D modeling.

5.3. Dynamical Masses

Using the inferred kinematic properties, we estimate the total amount of matter within the region probed by the CO line emission, i.e., the dynamical mass, M_{dyn}. For local galaxies, the dynamical mass is typically estimated from the circular motion, inferred from a rotation curve, and the maximum extent of the rotating disk, typically inferred from H I or stellar light profiles. In combination with measurements of the baryonic mass components (i.e., the stellar and gas mass), the dynamical mass can be applied to estimate the fraction of baryonic or dark matter within the observed region of the galaxy. Such estimates become highly uncertain for high-redshift galaxies, for which high-resolution observations of line kinematics are scarce, stellar and gas masses are highly uncertain, source sizes are challenging to constrain, and the inclination is often unknown. Moreover, even for galaxies for which the emission line observations are resolved, the observations typically do not extend to the radii required to infer the dynamical mass within the entire baryonic disk.

We infer the dynamical mass of all three galaxies, assuming that the bulk of the emission can be well described by a rotating disk (which appears consistent with the lines profiles, as discussed in Section 5.1). The correct choice of radius is somewhat arbitrary (often high-redshift studies use the rest-frame optical half-light radius or twice this value to estimate dynamical masses). Here, we estimate these values for two definitions of the maximum radius probed by the CO, twice the half-light radius $r_{max} = 2r_{1/2}^{CO}$ and six times the exponential scale length $r_{max} = 6r_d^{CO}$. For consistency with the inferred maximum rotation velocities, we estimate the outer radii using the half-light radii inferred using QUBEFIT (Table 5).

We determine the dynamical mass and total baryonic mass (stellar plus molecular gas mass) from within r_{max}, via

$$M_{dyn}(\leqslant r_{max}) = \frac{v_{rot}^2 \, r_{max}}{G}, \tag{5}$$

where v_{rot} is the modeled, rotation velocity, and G is the gravitational constant. We infer the total content of baryonic matter using the measured molecular gas and stellar masses in combination with the modeled surface brightness profiles of the CO and 1.6 μm emission, respectively. We estimate the fraction of light within r_{max}, from the 2D model profiles, and scale the molecular gas and stellar masses by the respective fractions. We thereby assume that the 1.6 μm emission perfectly traces the stellar mass, and that the excitation and CO-to-molecular gas mass conversion are constant over the entire galaxy disk. The dynamical and baryonic masses estimated for the three sources are provided in Table 5. For ALPS.2, we estimate a dynamical mass of $(2.7 \pm 0.3) \times 10^{11} M_\odot$ within $2r_{1/2}^{CO} \approx 9.2$ kpc, very close to the $M_{dyn} \sim 2.0 \times 10^{11} M_\odot$ inferred by Decarli et al. (2016) (from the initial 3 mm ASPECS data, based on the rest-frame optical half-light radius of 8.3 kpc).

As described in Section 3.2, a number of assumptions affect the inferred stellar masses. We therefore account for a factor of two uncertainty on the stellar mass (see Appendix B). The molecular gas masses are based on the assumption that the mass–metallicity relation holds for all three galaxies and that the α_{CO} conversion factor is purely a function of the metallicity and does not evolve with redshift. We include the uncertainties on the metallicity estimate and α_{CO} based on the uncertainties of the empirical relations used. We attempt to account for the uncertainty on the CO excitation. For ALPS.3 we use the measured line luminosity ratio, whereas for ALPS.1 and 2 we assume a CO(2–1)-to-CO(1–0) line ratio consistent with what has been previously measured for high-redshift sources. In addition, we assume that the ratio of $M_*/L_{1.6\,\mu m}$ is constant, and that the line ratios and α_{CO} are constant over the entire galaxy disk. Compared with other systematic uncertainties, radial variations in the applied ratios will have little impact on the derived baryonic masses and dark matter fractions. In addition to these uncertainties on the baryonic mass, the dynamical mass is heavily dependent on the inclination angle. We account for the range of inclination angles that fit the CO data in the uncertainties on the maximum rotation velocities.

Based on the dynamical and baryonic mass estimates, we estimate the dark matter fractions, $f_{DM} = 1 - M_{baryon}/M_{dyn}$, enclosed within the two types of maximum radii chosen here. For ALPS.2, we infer dark matter fractions of up to 70% and 80% (within 1σ), within $r_{1/2}^{CO}$ and $6r_d^{CO}$, respectively. We place
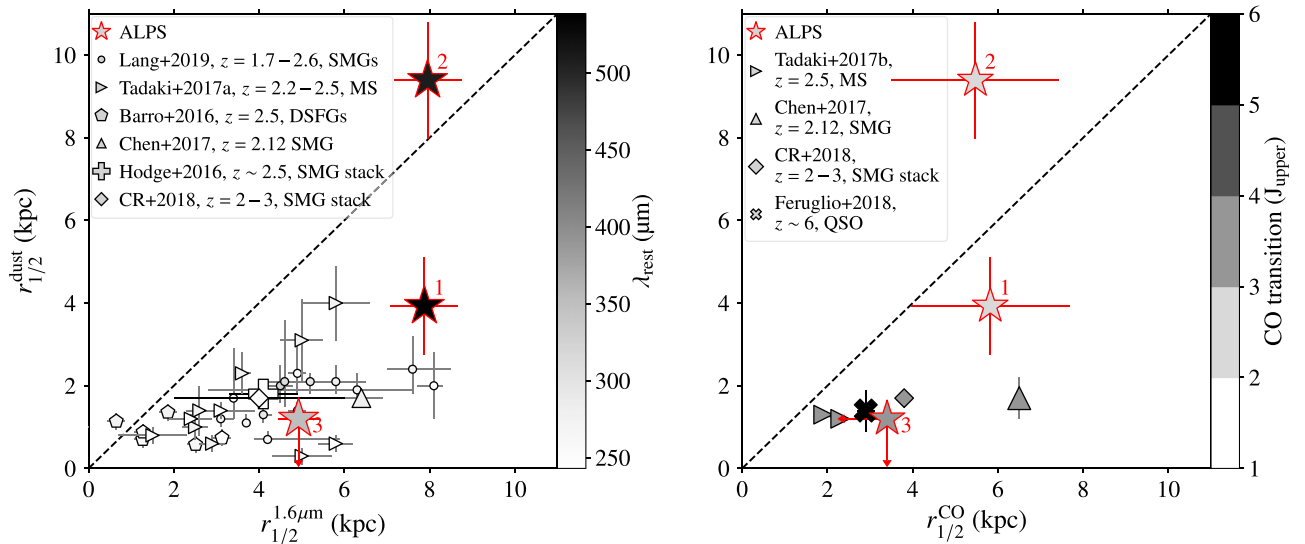
Figure 9. Comparison of the source sizes measured for our sample (stars) to other samples with dust-continuum size measurements (labeled in legends Barro et al. 2016; Hodge et al. 2016; Chen et al. 2017; Tadaki et al. 2017a, 2017b; Calistro Rivera et al. 2018; Feruglio et al. 2018; Lang et al. 2019). The source sizes shown here are measured from 2D maps using GALFIT (note that for the CO emission we also estimate sizes based on the 3D data as described in Section 5.2). Left panel: the dust half-light radii compared with the half-light radii measured from 1.6 μm emission. The grayscale of the points indicates the wavelength of the rest-frame dust-continuum emission. For most high-redshift galaxies observed to date, the dust continuum is more compact than the 1.6 μm emission. ALPS.2 is rare in that we measure equivalent dust and stellar half-light radii. Right panel: the dust half-light radii compared with the CO half-light radii. Here the grayscale indicates the upper level of the observed CO transition. As highlighted in this panel, very few high-redshift sources have the high-resolution observations of both CO and dust-continuum emission, which are needed to compare the relative spatial distributions.

2σ upper limits on the dark matter fractions of ALPS.1 and 3, as the measured values are consistent with 0.

6. Discussion

6.1. Comparing the Spatial Extent of CO, Dust, and Stellar Emission

We have measured the spatial extent of the 1.3 mm dust-continuum, CO line, and rest-frame optical emission of three star-forming galaxies at $z = 1.41$, 1.55, and 2.70. In this section, we discuss our findings and compare our results with simulations as well as previous observational studies of local and high-redshift galaxies. Although there is a wealth of high-resolution data available for local galaxies, few resolved observations exist of high-redshift sources that are not gravitationally lensed (summarized in Figure 9).

6.1.1. Limitations

We begin by noting that our data impose some limitations upon the methodology applied here. To estimate galaxy sizes, we fit a single disk component to all sets of data, assuming that the inferred half-light radius is representative of the entire disk. We do so because the resolution ($\sim$6 kpc for the CO) and sensitivity of the ALMA observations do not allow us to decompose the data into multiple components. However, stellar bulges are known to produce a steep, central rise for the rest-frame optical emission, and high central SFRs do the same for dust-continuum emission. Thus, local studies typically either decompose the stellar and continuum emission into a bulge and disk component, or omit the central few kpc when characterizing the scale length of the exponential disk (e.g., Muñoz-Mateos et al. 2009; Hunt et al. 2015; Casasola et al. 2017).

6.1.2. CO versus Rest-frame Optical Sizes

For all three galaxies, the CO half-light radii are at least 30% smaller than the rest-frame optical half-light radii (see Table 4). This difference appears to be slightly larger than what has been observed for most local and high-redshift galaxies. As for our sources, Casasola et al. (2017) find that the mean scale length of the CO(2–1) and CO(1–0) surface brightness profiles for their 18, face-on local galaxies is 20%–60% smaller ($\sim$40%, on average) than the mean scale length at 0.6 μm (equivalent to the observed-frame 1.6 μm for our $z \sim 1.5$ galaxies). However, for the local galaxies in the HERA CO line Extragalactic Survey (HERACLES, Leroy et al. 2009) and SINGS samples (Regan et al. 2006), the measured CO scale lengths are, on average, consistent with the scale lengths of the 3.6 μm emission, but range from half to almost twice the scale length of the stellar tracers. Similarly, recent studies of $z = 2 - 3$ SMGs find equivalent CO and rest-frame optical half-light radii (Chen et al. 2017; Calistro Rivera et al. 2018).

The relative size of the CO versus rest-frame optical emission depends on the observed CO transition and rest-frame wavelength. Results from the Physics at High Angular resolution in Nearby GalaxieS (Schinnerer et al. 2019) survey as well as from HERACLES (Leroy et al. 2009) indicate that the CO(2–1) emission is co-spatial with the CO(1–0) emission. However, the ratio of the line luminosities can vary between 0.6 and 1.0, with brighter CO(2–1) typically found in the centers of galaxies. Brighter, or more peaked, CO emission may therefore bias our inferred measurements to smaller radii, particularly because our observations are not sensitive to gas columns below $\sim$5 $\times$ 10^{21} cm^{-2} beam^{-1}. The comparison between CO and stellar disk sizes is also influenced by the observed wavelength of the stellar emission. Age gradients in the stellar population across the disk and/or increased effects of reddening in the central regions also lead to a decline in the measured radii from the UV to NIR (e.g., Peletier et al. 1994; de Jong 1996; Pompei & Natali 1997; MacArthur et al. 2003;

Möllenhoff et al. 2006; Fathi et al. 2010).[22] Thus, the size measured for the 1.6 μm emission is also likely to be smaller than the intrinsic size of the stellar disk.

6.1.3. Dust-Continuum versus Rest-frame Optical Sizes

We observe both compact and extended dust emission, among the three galaxies studied here. For ALPS.1 and 3, the 1.3 mm half-light radii are $(50 \pm 20)\%$ and $<70\%$ of the 1.6 μm half-light radii, respectively. In contrast, the 1.3 mm half-light radius of ALPS.2 is equivalent to that at 1.6 μm.

Like the rest-frame 350 μm emission studied here, the rest-frame 240 μm (observed-frame 870 μm) dust-continuum emission of ALPS.3 is very compact. Rujopakarn et al. (2019) analyze this emission at 0″03 resolution. By modeling the source emission in the uv-plane using two concentric, elliptical Gaussians, they find that the "extended" dust component is best described by a profile with a major axis FWHM of $\sim$3.6 $\pm$ 0.1 kpc, corresponding to a half-light radius of $\sim$1.8 kpc, similar to the half-light radius measured here for the rest-frame 350 μm emission (i.e., $<$1.2 kpc from the image plane and $\sim$1.2 $\pm$ 0.2 kpc from the uv-plane analysis). Assuming that the continuum emission can be modeled by a MBB with a temperature of 25 K and dust emissivity index of 1.8, the rest-frame 350 μm ASPECS LP measurement, $S_\nu = 1070 \pm 50$ μJy, extrapolates to a rest-frame 240 μm flux of $\sim$2890 $\pm$ 120 μJy. This is consistent with the 2780 $\pm$ 90 μJy measured by Rujopakarn et al. (2019), implying that the shorter wavelength observations have not missed a significant component of extended emission. Thus, the shorter wavelength data are further evidence that the dust component of ALPS.3 is very compact.

The spatial extent of the dust-continuum emission in ALPS.1 and 2 differs significantly, despite the two galaxies exhibiting similar rest-frame optical half-light radii and similar stellar masses and SFRs (Table 2). From the multiwavelength comparison in Figure 2, it would appear as though the dust-continuum emission traces the bright, central stellar component visible in the 0.6 and 1.6 μm images (second and third columns from the left) for ALPS.1, with no 1.3 mm emission above our detection limit visible for the southern tail of the optical emission. Conversely, the dust emission from ALPS.2 appears to coincide with the location of the clump-like, outer disk components visible in the 0.6 and 1.6 μm images (columns 2 and 3 of Figure 2), but not the central, red, stellar component. We also note that an additional blue clump is apparent to the north of the UV-NIR images of ALPS.2, which is not apparent in dust-continuum emission, but it is unclear if this is a fore- or background source.

The extended dust-continuum emission of ALPS.2 differs not only from what is observed for ALPS.1 and 3, but also from other high-redshift galaxies (Figure 9). In most of these, the dust emission is 2–4 times more compact than the stellar emission, e.g., for SMGs the 870 μm half-light radii are typically measured to be $\lesssim$3 kpc, whereas the 1.6 μm emission can extend to 8 kpc (Hodge et al. 2015, 2019; Simpson et al. 2015; Chen et al. 2017; Calistro Rivera et al. 2018; Gullberg et al. 2019; Lang et al. 2019). However, based on observations and radiative transfer models of local galaxies, extended dust disks with sizes comparable to the size of the stellar disk are the norm (Xilouris et al. 1999; Bianchi 2007; Muñoz-Mateos et al. 2009; Holwerda et al. 2012). This tension can be resolved by the fact that the dust-continuum

---

[22] We also find that the stellar half-light radii of our galaxies decrease by up to 20% from the observed-frame 1.25–1.6 μm emission, e.g., the 1.25 μm half-light radius of ALPS.2 is 9.8 $\pm$ 0.9 kpc, which is 20 $\pm$ 10% larger than the 1.6 μm size.

emission does not perfectly trace the bulk of the dust mass, but may be temperature-weighted and thus also sensitive to the sources of heating.

The dust-continuum emission may be very compact, if the central regions are dominated by starbursts (or AGN). Based on their FIRE simulations of high-redshift SMGs, Cochrane et al. (2019) find that the FIR continuum emission mostly stems from regions with high star formation rates, tracing both the central region as well as spiral arms. Similarly, based on Illustris TNG simulations of $1 < z < 3$ MS galaxies, G. Popping et al. (2020 in preparation), find that the 1.2 mm emission best traces the regions with high rates of star formation. Moreover, both studies find that the $\sim$1 mm dust half-light radii are typically smaller than the dust half-mass radii. These studies indicate that the centrally concentrated continuum emission observed for many high-redshift galaxies has traced the high star formation rates of the central regions.

6.1.4. CO versus Dust Continuum

Like the comparison to the rest-frame optical emission in the previous section, we find that the dust-continuum emission is more compact than the CO line emission from ALPS.1 and 3, but more extended than the CO emission from ALPS.2. The compact continuum emission, relative to the CO emission, appears consistent with previous observations of unlensed high-redshift galaxies (Chen et al. 2017; Tadaki et al. 2017b; Calistro Rivera et al. 2018; Feruglio et al. 2018), as summarized in Figure 9.

Despite the relative differences in the extent of the CO and dust-continuum emission, the molecular gas masses inferred based on the total dust-continuum flux densities, using the empirical calibration of Scoville et al. (2014), are consistent with those measured based on the total CO emission. Thus, even though the total dust-continuum luminosity may correlate well with the CO emission (yielding the same total gas mass estimates), the dust-continuum emission is not a straightforward tracer of the extended dust disk (see also Groves et al. 2015).

In addition to the impact of dust heating, other physical effects may contribute to the difference in the extent of the CO and dust-continuum emission. Significant increases in the GDR toward the outskirts of galaxies may result in measured size differences. Although some individual galaxies exhibit evidence for an increase in the GDR with radius (e.g., Bendo et al. 2010), for most local galaxies the measured variation appears negligible (Sandstrom et al. 2013). Differences in the temperature and opacity across the disk seem likely to play a larger role, as indicated by the comparison of radiative transfer models with both the stacked CO(3–2) and dust-continuum emission in Calistro Rivera et al. (2018). We note that the dust-continuum emission of ALPS.1 and 3 appear steeper than for ALPS.2, indicating more centralized heating in these galaxies. Although the X-ray observations and SED strongly imply the presence of a central AGN in ALPS.2, there is no evidence from the UV-to-NIR images or 1.3 mm dust continuum for increased heating in the center. Deeper, high-resolution continuum observations will help to shed light on this issue.

6.1.5. A Plausible Explanation for Compact Dust and CO Emission

The compact dust (and CO) observations for ALPS.1 and 3 are consistent with what would be observed for galaxies hosting nuclear starbursts. To illustrate this, we use two local galaxies hosting nuclear starbursts, NGC 253 and NGC 4945, as an example (see Appendix C). Like the galaxies studied here, both of
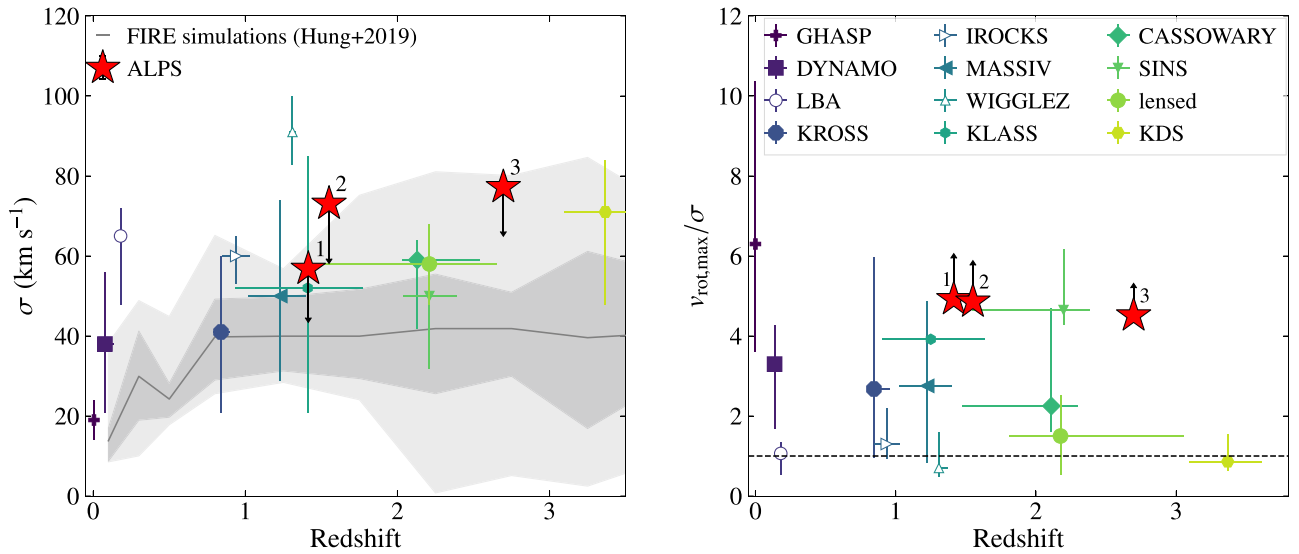
Figure 10. Left: Velocity dispersion as a function of redshift for star-forming galaxies. The solid gray line shows the median value for the simulated MS galaxies of Hung et al. (2019), with the dark and light gray regions enclosing 68% and 95% percent, respectively, of the simulated sources. The velocity dispersions of ALPS.1, 2, and 3, denoted by the red stars, are consistent with previous observations of MS galaxies. Right: comparison of the ratio of rotation-to-random motions for other galaxy samples. The colored symbols and errorbars in both panels indicate the median and 18th–64th percentiles of the GHASP survey (Epinat et al. 2010), DYNAMO survey (Green et al. 2014; Sweet et al. 2019), Lyman Break Analogues (LBA) (Gonçalves et al. 2010), KROSS (Harrison et al. 2017; Johnson et al. 2018), MASSIV (Epinat et al. 2012), WiggleZ survey (Wisnioski et al. 2011), KLASS (Mason et al. 2017), CASSOWARY (Leethochawalit et al. 2016), SINS (Cresci et al. 2009), lensed galaxies (Livermore et al. 2015), and KDS (Turner et al. 2017). The ALPS galaxies studied here have higher ratios of rotation-to-random motion than the majority of high-redshift galaxies observed to date. The velocity dispersion values for the comparison samples are provided in Table 2 of Hung et al. (2019). Observations for which the beam smearing is taken into account (for the rotation velocity) are shown as filled symbols (see Appendix A of Turner et al. 2017).

these local galaxies are heavily inclined and extended (with the 870 μm emission observed out to a radial distance of $\sim$7.5 kpc). Using the 870 μm LArge APEX BOlometer CAmera (LABOCA) observations of these two galaxies (Weiß et al. 2008), we create mock 1.3 mm maps with the same total flux density, resolution, and S/N as the data for ALPS.1, 2, and 3 presented here.

We find that the convolved size at half the peak surface brightness of the mock 1.3 mm maps (blue contours) matches the beam of our 1.3 mm data (Figure C1), due to the high contrast between the central, dust-continuum emission and that of the disk (up to a factor of 50 for NGC 4959). With the S/N and resolution of the data for ALPS.1 and 2, the spiral arms of NGC 253 would not be detected (at $>3\sigma$) and only the brightest spiral of NGC 4959 would be detected, making the observations appear asymmetric (similar to the 1.3 mm maps of ALPS.1 and 2 in Figure 2). The fact that we observe no extended structure in the 1.3 mm emission of ALPS.3 implies that the disk is less extended and/or the contrast between the nuclear and disk regions is even greater than for these two local starbursts. The comparison to these simple mock observations is consistent with the fact that our 1.3 mm observations are sensitive to a gas column of $N_{H_2} \sim 10^{22}$ cm^{-2}, whereas the column densities measured for most of the spiral arms regions of NGC 253 are significantly lower.

6.2. Dynamical Properties

We have measured the dynamical properties of all three sources, and conclude that the gas motion of each disk is dominated by rotation. The measured velocity dispersions are consistent with the measurements from the KLASS[23], CASSOWARY[24], KROSS[25], and SINS[26] surveys of galaxies

---
[23] KMOS Lens-Amplied Spectroscopic Survey (KLASS).
[24] The Cambridge And Sloan Survey Of Wide ARcs in the skY (CASSOWARY).
[25] KMOS Redshift One Spectroscopic Survey (KROSS).
[26] Spectroscopic Imaging survey in the Near-infrared with SINFONI (SINS).

at $1 < z < 3$ (Cresci et al. 2009; Leethochawalit et al. 2016; Mason et al. 2017; Johnson et al. 2018) and the simulations of Hung et al. (2019) (Figure 10). However, the maximum rotation velocities are greater than the majority of high-redshift galaxies in these samples. Thus, the rotation-to-random motions measured for our sample are higher than what has been been measured for most other high-redshift, star-forming galaxies (Figure 10) but consistent with the range of values typical of local disks (Epinat et al. 2010). It is unsurprising that the three galaxies studied here appear more rotation-dominated than most high-redshift galaxies studied to date, because our selection of extended and inclined sources favors "thin" rotating disks.

We note that ALPS.2 was also observed as part of the SINS sample (labeled GMASS 1084 in Förster Schreiber et al. 2009). Based on their Hα observations, Förster Schreiber et al. (2009) measure a rotation-to-dispersion ratio of $v_{rot}/\sigma = 4.4 \pm 2.1$, consistent with the $v_{rot}/\sigma = 4.9 \pm 0.9$ derived here. However, using the intrinsic, inclination-corrected rotation curve of the best-fitting model disk, they infer a lower circular velocity of $v_d = 230 \pm 38$ km s^{-1}. This lower velocity, compared with the 355 ± 14 km s^{-1} measured here, is consistent with the smaller half-light radius of the Hα emission compared with that of CO (3.1 ± 1 kpc versus 4.6 ± 0.3 kpc), assuming that the rotation curve is still rising.

To compare to the literature, we inferred the dark matter fractions of our sample from within two sets of outer radii, i.e., out to twice the CO half-light radii, $2r_{1/2}$, and to six times the CO exponential scale length, $6r_d$. For ALPS.1 and 3, the dynamical mass is of the same order as the baryonic mass, suggesting that the baryonic matter dominates at small radii. Even supposing that the molecular-to-gas mass conversion is overestimated by a factor of $\sim$4, this would still be the case. In contrast, for ALPS.2, the measured dark matter fraction within $2r_{1/2}^{CO(2-1)}$ is consistent with most simulations and local

observations (Lelli et al. 2016; Lovell et al. 2018; Tortora et al. 2019). It is also consistent with the dark matter fractions inferred from the high-redshift observations of Molina et al. (2019) and the $0.6 < z < 2.2$ galaxies of Tiley et al. (2019). The smaller inferred dark matter fractions of ALPS.1 and 3, compared to ALPS.2, are likely related to the more centrally concentrated molecular gas and stellar components. It is possible that these data simply do not extend far enough to measure the maximum radial velocities.

7. Summary

We have compared ALMA and HST observations, tracing the stellar, dust, and molecular gas components of three star-forming galaxies, ALPS.1 at $z = 1.41$, ALPS.2 at $z = 1.55$, and ALPS.3 at $z = 2.70$. These galaxies were selected from the ASPECS LP, based on their bright CO and dust-continuum emission and their large, rest-frame optical sizes. Our main findings can be summarized as follows.

1. Our ALMA observations appear to trace the presence of nuclear starbursts, but are barely sensitive to extended spiral structure. For all three galaxies, the CO emission appears $\gtrsim 30\%$ more compact than the rest-frame optical emission. The 1.3 mm emission also appears more compact, by at least a factor of two, than the rest-frame optical emission of ALPS.1 and 3. In contrast, the 1.3 mm emission of ALPS.2 appears as extended as the rest-frame optical, albeit at poor S/N. The compact CO versus rest-frame optical emission implies the presence of a central, dense ISM component. Similarly, the compact 1.3 mm emission of ALPS.1 is consistent with what would be observed for an extended disk galaxy hosting a nuclear starburst, tracing a high central gas column density (and potentially also a high central star formation rate). For both the CO and 1.3 mm observations, temperature gradients would only serve to further increase the contrast between the nuclear region and the more extended disks. Compared with ALPS.1, the more extended 1.3 mm (versus 1.6 μm) emission of ALPS.2 may imply the existence of denser spiral structure at large radii. However, higher S/N data are needed to confirm this result.

2. Our observations of ALPS.3 imply that there may exist a population of sources where the vast majority of the gas and dust is within a compact, nuclear starburst region. Both the CO and dust-continuum observations are significantly more compact than the rest-frame optical emission, with no structure recovered at $\geqslant 3\sigma$ beyond ~ 2 kpc. For observations at the sensitivity and resolution of the 1.3 mm data for ALPS.3, we would expect to be able to observe dense spiral structure with a column density of $N_{H_2} \sim 10^{22}$ cm^{-2} averaged over our synthesized beam, a value typical for extended local disk galaxies.

3. We investigate the dynamical properties of the three galaxies, based on our resolved observations of the CO(2–1) and CO(3–2) line emission. Our analysis indicates that the gas motion of all three galaxies is rotation-dominated. Based on the kinematic properties, we infer the dynamical masses and dark matter fractions within the region traced by the CO emission. Assuming CO-to-molecular gas conversion factors consistent with that of the Milky Way, we infer dark matter fractions of up to 0.6, consistent with simulations and observations of local galaxies with the same stellar masses.

We conclude with a note of caution. Based on our analysis, we find that measurements of the dust and CO half-light radii are still hampered by low-sensitivity observations. We barely recover the extended cool dust component for one source and only observe the CO emission out to ~ 10 kpc, despite substantial time investments with ALMA. At 3σ our data are sensitive to a molecular gas column density of 10^{22} cm^{-2} per beam. Thus, we miss regions of gas that are less dense than this and/or smaller than the synthesized beam. To triple the sensitivity of the observations would require a tenfold increase in the ALMA time per source, for both the CO and continuum emission. Thus, significant additional investments with ALMA are required to observe the extended gas and dust disks of high-redshift galaxies.

Appendix A
Additional Target

Along with ALPS.3, we observe an additional galaxy at an angular separation of 7.″56. The additional source is labeled 3 mm.09, in the 3 mm ASPECS Large Program González-

HST - rgb   HST - F606W   HST - F160W   ALMA - Band 6 dust continuum   ALMA - Band 3 CO Moment 0   VLA - 5cm
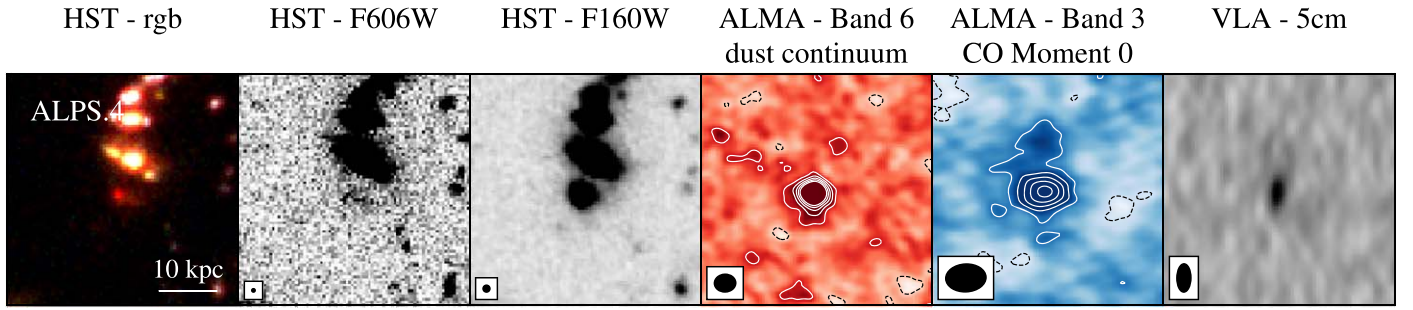
Figure A1. Multiwavelength data for the additional source, ASPECS LP 3 mm.09, observed with ALPS.3. The dust-continuum and CO emission are unresolved and the source appears compact in the rest-frame optical (columns 1-3). Each panel depicts a $5'' \times 5''$ region centered on the HST-defined center of the source. Columns, from left to right: HST 435/775/105 color composite, HST/F606W, HST/F160W, Band 6 (1.3 mm) dust continuum (combined ASPECS and Dunlop et al. 2017 data), CO moment-0 map (from the combined ASPECS and ALPS data), and VLA—5 cm continuum flux. The contours for the Band 6 dust continuum and CO moment 0 start at $\pm 2\sigma$ and change in steps of 2σ. Dashed black (solid white) lines show negative (positive) contours.

López et al. (2019) and UDF1 in the the 1.3 mm program of Dunlop et al. (2017). The galaxy is classified as an AGN, based on the X-ray observations of Luo et al. (2017), and has a molecular gas to stellar mass fraction around unity (Boogaard et al. 2019). We show the HST data along with our ALMA observations and the 5 cm continuum in Figure A1. Resolved observations of this source, at 870 μm, are presented and discussed in Rujopakarn et al. (2019). They also model the HST H160 emission, which they find is best fit by the combination of a bright point source and fainter Sérsic component with a half-light radius of 3.16 ± 0.17 kpc (potentially representing the AGN and disk, respectively). The centroid of the 870 μm emission (Rujopakarn et al. 2019) and the 1.3 mm data presented here is co-located with the AGN/point source. We find no evidence for resolved CO or 1.3 mm continuum emission for this source, nor do we find any evidence for rotation based on the channel maps or position–velocity diagrams.

The CO data for this source show both the compact region observed in the 1.3 mm dust continuum as well as an additional CO emitting region to the north, detected at $\gtrsim 3\sigma$. The northern region may be an additional CO emitter, which matches the position of the MUSE absorption line at the same redshift (presented and discussed in Figure 2 and Appendix A of Boogaard et al. 2019). This additional or adjoined source exhibits a red core in the HST images but is barely apparent in the rest-frame UV images and is not observed in the 870 μm data of Rujopakarn et al. (2019).

Appendix B
SED Analysis

We briefly elaborate on some of the details of the SED modeling for our sources here.

To model the SEDs, we rely on the accuracy of the measured photometry. Two catalogs of photometry are available for the HUDF, spanning from the UV to the mid-IR (Spitzer IRAC), those of Guo et al. (2013), and the 3D-HST catalog described in Skelton et al. (2014). The HST fluxes from the two HUDF catalogs vary significantly across different bands for our sources. Although both Guo et al. (2013) and Skelton et al. (2014) extract fluxes from HST images matched to the source-detection image (the HST F160W Band for our sources), their chosen aperture sizes differ. Skelton et al. (2014) extract the source flux from circular apertures of $0''7$ diameter, whereas Guo et al. (2013) infer the total flux from the isophotal area

(i.e., the detection footprint in the F160W image), The sources investigated here exhibit extended rest-frame optical emission, with F160W half-light radii of $0''6$–$0''98$ (see Table 2). Thus, the 3D-HST measurements underestimate the flux of our sources, especially at shorter wavelengths (in the UV). We therefore choose to use the HST and Spitzer/IRAC photometry from the Guo et al. (2013) catalog, which are consistent with the fluxes inferred from the XDF images using circular apertures enclosing our sources (cyan shaded regions and circles in Figure 3). For ALPS.1 and 2 the stellar masses inferred based on the Guo et al. (2013) catalog are a factor of 1.5 times lower than inferred from the Skelton et al. (2014) catalog, whereas the SFRs are 1.5 times greater. Conversely, for ALPS.3 the Guo et al. (2013) photometry results in a stellar mass 1.5 times greater and SFR 1.5 times smaller than when using the Skelton et al. (2014) photometry.

To model the SEDs, use the MAGPHYS algorithm. MAGPHYS simulates the stellar emission of a galaxy using population synthesis models, based on a variety of star formation histories (SFHs), and links the stellar energy absorbed and scattered by dust grains to the energy of the thermal emission. As discussed in Buat et al. (2019) and Battisti et al. (2019), the assumptions used to link the stellar and dust emission, such as a simple SFH and dust attenuation recipe, can significantly bias the derived parameters. Attenuation curves vary between galaxies (e.g., Salmon et al. 2016; Buat et al. 2018; Salim et al. 2018) and flatten when the amount of obscuration or SFR increase (e.g., Jonsson et al. 2010; Chevallard et al. 2013; Roebuck et al. 2019).

In this work we have adopted two adapted versions of the MAGPHYS algorithm as the fits using the standard high-redshift MAGPHYS algorithm left significant residuals. We apply the version of Battisti et al. (2019) to ALPS.1 and 3. This adapted version includes a SFH that both rises linearly at early ages and then declines exponentially (whereas before it was an exponentially declining function), has broader priors on the range of optical dust depths and equilibrium dust temperatures (to reflect high-redshift observations, particularly of sub-mm galaxies), includes a prescription for absorption by the intergalactic medium, and includes an additional component in the attenuation curve for the diffuse (ISM) to characterize the attenuation due to the 2175 Å feature.

We test the extent to which the inferred stellar masses and SFRs depend on different photometric bands. Based on the omission of different bands, we find that the peak of the near-infrared emission is particularly important in the stellar mass

fits, i.e., the SED fits are highly sensitive to the IRAC photometry, particularly for ALPS.3. For ALPS.1, 2, and 3, respectively, omitting the IRAC photometry resulted in an inferred median stellar masses of ~1.5, ~3, and ~5 times smaller than the median values inferred when using the full set of photometry.

Multiple assumptions systematically bias the inferred stellar masses and SFRs, including the choice of aperture size for the HST photometry (which change the inferred stellar masses by a factor of 1.5–2), our reliance on the accuracy of photometry at the peak of the stellar-continuum emission (which change the inferred stellar masses by a factor of 1.5–5), the inclusion of an unconstrained AGN component (which change the inferred stellar masses by a factor of ~2 for $\xi_{AGN} \sim 0.15$), and the applied dust attenuation curve (which also changes the inferred stellar masses by a factor of ~1.5–2). Based on these systematics, we adopt an uncertainty floor of ±0.3 dex on the stellar masses and SFRs inferred here.

Appendix C
Local Starbursts

To place the measured sizes for our data in context, we create mock 1.3 mm maps of two local galaxies that harbor nuclear starbursts, NGC 253 and NGC 4945. We use the 870 μm LABOCA maps from Weiß et al. (2008), smooth these to the resolution of the Band 6 data, scale the flux to match the total flux density of each of our sources, and add the same level of noise as for our data (smoothed to the beam). We thereby assume that the distribution of the rest frame 870 μm matches that of the rest-frame 540, 509, and 350 μm emission, respectively, for ALPS.1, 2, and 3. The results are shown in Figure C1. The mock observations are barely resolved, with the observed size at half the peak surface brightness (blue contours) matching the 1.3 mm beam size. Only a portion of the brightest spiral arms appear to be recovered at $>3\sigma$.
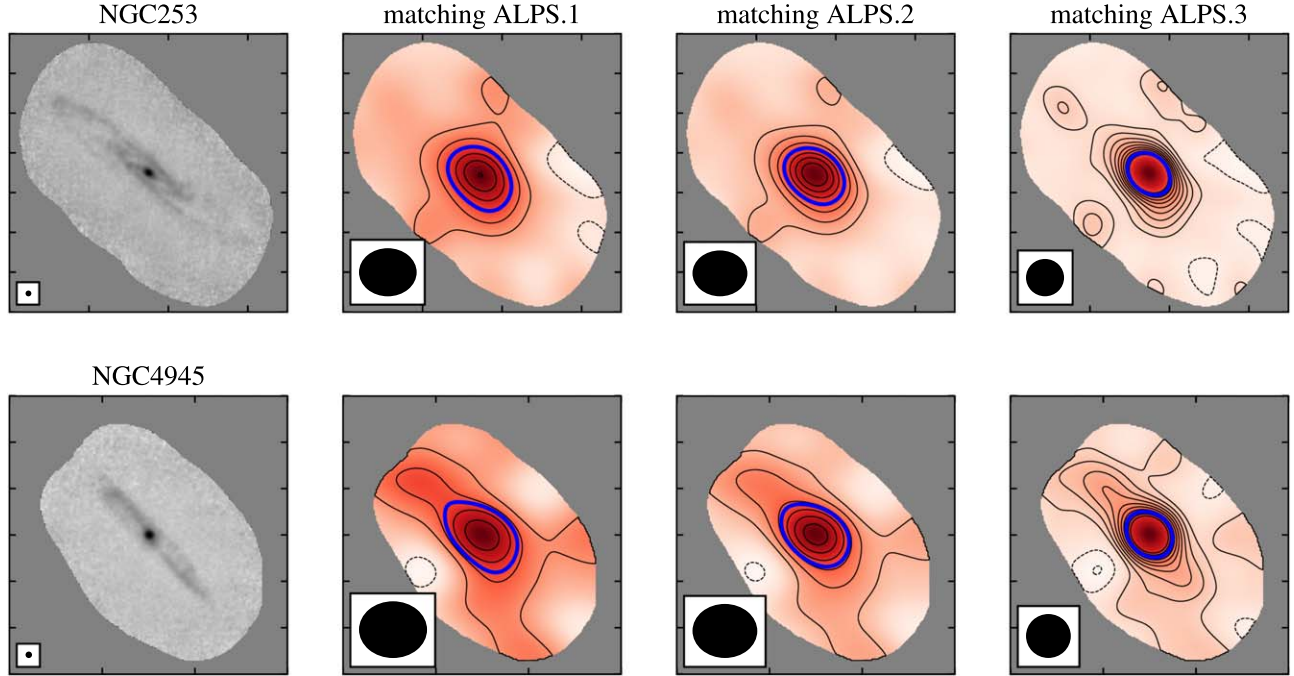
Figure C1. Mock observations of the local active galaxies, NGC 253 and NGC 4959, matching the total dust mass (i.e., measured flux) to the sources observed here. Left column: original LABOCA observations. Second to fourth column: mock 1.3 mm observations matching the rms and total flux density of ALPS.1, 2, and 3 respectively. Contours start at $\pm 2\sigma$ and go in steps of 2σ. Solid (dashed) lines show positive (negative) contours. The half-peak emission contours are shown in blue.

ORCID iDs

Melanie Kaasinen ⓘ https://orcid.org/0000-0002-1173-2579
Fabian Walter ⓘ https://orcid.org/0000-0003-4793-7880
Mladen Novak ⓘ https://orcid.org/0000-0001-8695-825X
Marcel Neeleman ⓘ https://orcid.org/0000-0002-9838-8191
Ian Smail ⓘ https://orcid.org/0000-0003-3037-257X
Leindert Boogaard ⓘ https://orcid.org/0000-0002-3952-8588
Elisabete da Cunha ⓘ https://orcid.org/0000-0001-9759-4797
Axel Weiss ⓘ https://orcid.org/0000-0003-4678-3939
Daizhong Liu ⓘ https://orcid.org/0000-0001-9773-7479
Roberto Decarli ⓘ https://orcid.org/0000-0002-2662-8803
Gergö Popping ⓘ https://orcid.org/0000-0003-1151-4659
Tanio Diaz-Santos ⓘ https://orcid.org/0000-0003-0699-6083
Paulo Cortés ⓘ https://orcid.org/0000-0002-3583-780X
Manuel Aravena ⓘ https://orcid.org/0000-0002-6290-3198
Paul van der Werf ⓘ https://orcid.org/0000-0001-5434-5942
Dominik Riechers ⓘ https://orcid.org/0000-0001-9585-1462
Hanae Inami ⓘ https://orcid.org/0000-0003-4268-0393
Jacqueline A. Hodge ⓘ https://orcid.org/0000-0001-6586-8845
Hans-Walter Rix ⓘ https://orcid.org/0000-0003-4996-9069

References

Aravena, M., Boogaard, L., Gónzalez-López, J., et al. 2020, arXiv:2006.04284
Aravena, M., Decarli, R., Gónzalez-López, J., et al. 2019, ApJ, 882, 136
Astropy Collaboration, Robitaille, T. P., Tollerud, E. J., et al. 2013, A&A, 558, A33
Barro, G., Kriek, M., Pérez-González, P. G., et al. 2016, ApJL, 827, L32
Battisti, A. J., da Cunha, E., Grasha, K., et al. 2019, ApJ, 882, 61
Bendo, G. J., Wilson, C. D., Warren, B. E., et al. 2010, MNRAS, 402, 1409
Bianchi, S. 2007, A&A, 471, 765
Bianchi, S., & Xilouris, E. M. 2011, A&A, 531, L11
Blain, A. W., Smail, I., Ivison, R. J., Kneib, J. P., & Frayer, D. T. 2002, PhR, 369, 111
Bolatto, A. D., Warren, S. R., Leroy, A. K., et al. 2015, ApJ, 809, 175
Boogaard, L. A., Brinchmann, J., Bouché, N., et al. 2018, A&A, 619, A27
Boogaard, L. A., Decarli, R., Gónzalez-López, J., et al. 2019, ApJ, 882, 140
Boogaard, L., van der Werf, P., Weiß, A., et al. 2020, ApJ, submitted
Bothwell, M. S., Smail, I., Chapman, S. C., et al. 2013, MNRAS, 429, 3047
Buat, V., Boquien, M., Małek, K., et al. 2018, A&A, 619, A135
Buat, V., Ciesla, L., Boquien, M., Małek, K., & Burgarella, D. 2019, A&A, 632, A79
Calistro Rivera, G., Hodge, J. A., Smail, I., et al. 2018, ApJ, 863, 56
Casasola, V., Cassarà, L. P., Bianchi, S., et al. 2017, A&A, 605, A18
Casey, C. M., Narayanan, D., & Cooray, A. 2014, PhR, 541, 45
Catinella, B., Schiminovich, D., Kauffmann, G., et al. 2010, MNRAS, 403, 683
Chabrier, G. 2003, PASP, 115, 763
Chang, Y.-Y., Le Floc'h, E., Juneau, S., et al. 2020, ApJ, 888, 44
Chen, C.-C., Hodge, J. A., Smail, I., et al. 2017, ApJ, 846, 108
Chevallard, J., Charlot, S., Wandelt, B., & Wild, V. 2013, MNRAS, 432, 2061
Cochrane, R. K., Hayward, C. C., Anglés-Alcázar, D., et al. 2019, MNRAS, 488, 1779
Conselice, C. J. 2003, ApJS, 147, 1
Conselice, C. J., Bershady, M. A., & Jangren, A. 2000, ApJ, 529, 886
Cresci, G., Hicks, E. K. S., Genzel, R., et al. 2009, ApJ, 697, 115
da Cunha, E., Charlot, S., & Elbaz, D. 2008, MNRAS, 388, 1595
da Cunha, E., Walter, F., Smail, I. R., et al. 2015, ApJ, 806, 110
Daddi, E., Dannerbauer, H., Liu, D., et al. 2015, A&A, 577, A46
de Blok, W. J. G., & Walter, F. 2014, AJ, 147, 96
de Jong, R. S. 1996, A&A, 313, 377
Decarli, R., Walter, F., Aravena, M., et al. 2016, ApJ, 833, 70
Decarli, R., Walter, F., Gónzalez-López, J., et al. 2019, ApJ, 882, 138
Decarli, R., Walter, F., Venemans, B. P., et al. 2018, ApJ, 854, 97
Di Teodoro, E. M., & Fraternali, F. 2015, MNRAS, 451, 3021
Draine, B. T., & Lee, H. M. 1984, ApJ, 285, 89
Dunlop, J. S., McLure, R. J., Biggs, A. D., et al. 2017, MNRAS, 466, 861
Elbaz, D., Dickinson, M., Hwang, H. S., et al. 2011, A&A, 533, A119
Epinat, B., Amram, P., Balkowski, C., & Marcelin, M. 2010, MNRAS, 401, 2113
Epinat, B., Tasca, L., Amram, P., et al. 2012, A&A, 539, A92
Fathi, K., Allen, M., Boch, T., Hatziminaoglou, E., & Peletier, R. F. 2010, MNRAS, 406, 1595
Feruglio, C., Fiore, F., Carniani, S., et al. 2018, A&A, 619, A39
Förster Schreiber, N. M., Genzel, R., Bouché, N., et al. 2009, ApJ, 706, 1364
Franco, M., Elbaz, D., Zhou, L., et al. 2020, arXiv:2005.03040
Genzel, R., Tacconi, L. J., Lutz, D., et al. 2015, ApJ, 800, 20
Gildas Team. 2013, GILDAS: Grenoble Image and Line Data Analysis Software, Astrophysics Source Code Library, ascl:1305.010
Gonçalves, T. S., Basu-Zych, A., Overzier, R., et al. 2010, ApJ, 724, 1373
González-López, J., Decarli, R., Pavesi, R., et al. 2019, ApJ, 882, 139
González-López, J., Novak, M., Decarli, R., et al. 2020, ApJ, 897, 91
Green, A. W., Glazebrook, K., McGregor, P. J., et al. 2014, MNRAS, 437, 1070
Groves, B. A., Schinnerer, E., Leroy, A., et al. 2015, ApJ, 799, 96
Gullberg, B., Smail, I., Swinbank, A. M., et al. 2019, MNRAS, 490, 4956
Guo, Y., Ferguson, H. C., Giavalisco, M., et al. 2013, ApJS, 207, 24
Haas, M., Lemke, D., Stickel, M., et al. 1998, A&A, 338, L33
Harrison, C. M., Johnson, H. L., Swinbank, A. M., et al. 2017, MNRAS, 467, 1965
Hodge, J. A., & da Cunha, E. 2020, arXiv:2004.00934
Hodge, J. A., Riechers, D., Decarli, R., et al. 2015, ApJL, 798, L18
Hodge, J. A., Smail, I., Walter, F., et al. 2019, ApJ, 876, 130
Hodge, J. A., Swinbank, A. M., Simpson, J. M., et al. 2016, ApJ, 833, 103
Holwerda, B. W., Bianchi, S., Böker, T., et al. 2012, A&A, 541, L5
Hung, C.-L., Hayward, C. C., Yuan, T., et al. 2019, MNRAS, 482, 5125
Hunt, L. K., Draine, B. T., Bianchi, S., et al. 2015, A&A, 576, A33
Hunter, J. D. 2007, CSE, 9, 90
Illingworth, G. D., Magee, D., Oesch, P. A., et al. 2013, ApJS, 209, 6
Johnson, H. L., Harrison, C. M., Swinbank, A. M., et al. 2018, MNRAS, 474, 5076
Jonsson, P., Groves, B. A., & Cox, T. J. 2010, MNRAS, 403, 17
Kaasinen, M., Scoville, N., Walter, F., et al. 2019, ApJ, 880, 15
Kewley, L. J., & Ellison, S. L. 2008, ApJ, 681, 1183
Lang, P., Schinnerer, E., Smail, I., et al. 2019, ApJ, 879, 54
Leethochawalit, N., Jones, T. A., Ellis, R. S., et al. 2016, ApJ, 820, 84
Lelli, F., McGaugh, S. S., & Schombert, J. M. 2016, AJ, 152, 157
Leroy, A. K., Walter, F., Bigiel, F., et al. 2009, AJ, 137, 4670
Leroy, A. K., Walter, F., Brinks, E., et al. 2008, AJ, 136, 2782
Leslie, S., Schinnerer, E., Liu, D., et al. 2020, arXiv:2006.13937
Liu, D., Schinnerer, E., Groves, B., et al. 2019, ApJ, 887, 235
Livermore, R. C., Jones, T. A., Richard, J., et al. 2015, MNRAS, 450, 1812
Lovell, M. R., Pillepich, A., Genel, S., et al. 2018, MNRAS, 481, 1950
Luo, B., Brandt, W. N., Xue, Y. Q., et al. 2017, ApJS, 228, 2
MacArthur, L. A., Courteau, S., & Holtzman, J. A. 2003, ApJ, 582, 689
Martí-Vidal, I., Vlemmings, W. H. T., Muller, S., & Casey, S. 2014, A&A, 563, A136
Mason, C. A., Treu, T., Fontana, A., et al. 2017, ApJ, 838, 14
McMullin, J. P., Waters, B., Schiebel, D., Young, W., & Golap, K. 2007, in ASP Conf. Ser. 376, Astronomical Data Analysis Software and Systems XVI, ed. R. A. Shaw, F. Hill, & D. J. Bell (San Francisco, CA: ASP), 127
Molina, J., Ibar, E., Smail, I., et al. 2019, MNRAS, 487, 4856
Möllenhoff, C., Popescu, C. C., & Tuffs, R. J. 2006, A&A, 456, 941
Muñoz-Mateos, J. C., Gil de Paz, A., Boissier, S., et al. 2009, ApJ, 701, 1965
Neeleman, M., Bañados, E., Walter, F., et al. 2019, ApJ, 882, 10
Nelson, E. J., Tadaki, K.-i., Tacconi, L. J., et al. 2019, ApJ, 870, 130
Noeske, K. G., Weiner, B. J., Faber, S. M., et al. 2007, ApJL, 660, L43
Novak, M., Bañados, E., Decarli, R., et al. 2019, ApJ, 881, 63
Pavesi, R., Sharon, C. E., Riechers, D. A., et al. 2018, ApJ, 864, 49
Peletier, R. F., Valentijn, E. A., Moorwood, A. F. M., & Freudling, W. 1994, A&AS, 108, 621
Peng, C. Y., Ho, L. C., Impey, C. D., & Rix, H.-W. 2002, AJ, 124, 266
Peng, C. Y., Ho, L. C., Impey, C. D., & Rix, H.-W. 2010, AJ, 139, 2097
Pettini, M., & Pagel, B. E. J. 2004, MNRAS, 348, L59
Pety, J. 2005, in SF2A-2005: Semaine de l'Astrophysique Francaise, ed. F. Casoli et al. (Les Ulis: EdP-Sciences), 721
Planck Collaboration, Abergel, A., Ade, P. A. R., et al. 2011, A&A, 536, A21
Pompei, E., & Natali, G. 1997, A&AS, 124, 129
Regan, M. W., Thornley, M. D., Vogel, S. N., et al. 2006, ApJ, 652, 1112
Reid, R. I. 2010, AAS Meeting Abstracts, 42, 479.04
Riechers, D. A., Boogaard, L. A., Decarli, R., et al. 2020, ApJL, 896, L21
Roebuck, E., Sajina, A., Hayward, C. C., et al. 2019, ApJ, 881, 18
Rujopakarn, W., Daddi, E., Rieke, G. H., et al. 2019, ApJ, 882, 107
Salim, S., Boquien, M., & Lee, J. C. 2018, ApJ, 859, 11
Salmi, F., Daddi, E., Elbaz, D., et al. 2012, ApJL, 754, L14
Salmon, B., Papovich, C., Long, J., et al. 2016, ApJ, 827, 20

Sandstrom, K. M., Leroy, A. K., Walter, F., et al. 2013, ApJ, 777, 5
Schinnerer, E., Leroy, A., Blanc, G., et al. 2019, Msngr, 177, 36
Schreiber, C., Elbaz, D., Pannella, M., et al. 2016, A&A, 589, A35
Schreiber, C., Pannella, M., Elbaz, D., et al. 2015, A&A, 575, A74
Scoville, N., Aussel, H., Sheth, K., et al. 2014, ApJ, 783, 84
Scoville, N., Lee, N., Vanden Bout, P., et al. 2017, ApJ, 837, 150
Simpson, J. M., Smail, I., Swinbank, A. M., et al. 2015, ApJ, 799, 81
Skelton, R. E., Whitaker, K. E., Momcheva, I. G., et al. 2014, ApJS, 214, 24
Solomon, P. M., Downes, D., & Radford, S. J. E. 1992, ApJL, 398, L29
Speagle, J. S., Steinhardt, C. L., Capak, P. L., & Silverman, J. D. 2014, ApJS, 214, 15
Spilker, J. S., Marrone, D. P., Aguirre, J. E., et al. 2014, ApJ, 785, 149
Stach, S. M., Dudzevičiūtė, U., Smail, I., et al. 2019, MNRAS, 487, 4648
Sweet, S. M., Fisher, D. B., Savorgnan, G., et al. 2019, MNRAS, 485, 5700
Swinbank, A. M., Simpson, J. M., Smail, I., et al. 2014, MNRAS, 438, 1267
Tacconi, L. J., Genzel, R., Saintonge, A., et al. 2018, ApJ, 853, 179
Tacconi, L. J., Neri, R., Genzel, R., et al. 2013, ApJ, 768, 74
Tadaki, K.-i., Genzel, R., Kodama, T., et al. 2017a, ApJ, 834, 135
Tadaki, K.-i., Kodama, T., Nelson, E. J., et al. 2017b, ApJL, 841, L25

Taylor, M. B. 2005, in ASP Conf. Ser. 347, Astronomical Data Analysis Software and Systems XIV, ed. P. Shopbell, M. Britton, & R. Ebert (San Francisco, CA: ASP), 29
Tiley, A. L., Swinbank, A. M., Harrison, C. M., et al. 2019, MNRAS, 485, 934
Tortora, C., Posti, L., Koopmans, L. V. E., & Napolitano, N. R. 2019, MNRAS, 489, 5483
Turner, O. J., Cirasuolo, M., Harrison, C. M., et al. 2017, MNRAS, 471, 1280
van der Wel, A., Bell, E. F., Häussler, B., et al. 2012, ApJS, 203, 24
Walter, F., Decarli, R., Aravena, M., et al. 2016, ApJ, 833, 67
Wang, F., Wang, R., Fan, X., et al. 2019, ApJ, 880, 2
Wang, R., Wagg, J., Carilli, C. L., et al. 2013, ApJ, 773, 44
Weiß, A., Kovács, A., Güsten, R., et al. 2008, A&A, 490, 77
Whitaker, K. E., Franx, M., Leja, J., et al. 2014, ApJ, 795, 104
Whitaker, K. E., van Dokkum, P. G., Brammer, G., & Franx, M. 2012, ApJL, 754, L29
Williams, R. J., Maiolino, R., Santini, P., et al. 2014, MNRAS, 443, 3780
Willott, C. J., Bergeron, J., & Omont, A. 2015, ApJ, 801, 123
Wisnioski, E., Glazebrook, K., Blake, C., et al. 2011, MNRAS, 417, 2601
Xilouris, E. M., Byun, Y. I., Kylafis, N. D., Paleologou, E. V., & Papamastorakis, J. 1999, A&A, 344, 868